AD-A254 049

IIIIIIIIIIIIIIIIIIIIIIIIII

NASA TECHNICAL MEMORANDUM 107623
AVSCOM TECHNICAL REPORT 92-B-008

AN INTERLAMINAR TENSION
STRENGTH SPECIMEN

Wade C. Jackson and Roderick H. Martin

DTIC
ELECTE
AUG 19 1992
S D

May 1992
Paper presented at the ASTM 11th Symposium on Composite
Materials: Testing and Design, Pittsburgh, PA, May 4-5, 1992

NASA

US ARMY
AVIATION
SYSTEMS COMMAND
AVIATION R&T ACTIVITY

92-22978

IIIIIIIIIIIIIIIIIIIIII

92 8 18 029

Abstract

This paper describes a technique to determine interlaminar tension strength, σ_{3c}, of a fiber reinforced composite material using a curved beam. The specimen was a unidirectional curved beam, bent 90°, with straight arms. Attached to each arm was a hinged loading mechanism which was held by the grips of a tensile testing machine. Geometry effects of the specimen, including the effects of loading arm length, inner radius, thickness, and width, were studied. The data sets fell into two categories: low strength corresponding to a macroscopic flaw related failure and high strength corresponding to a microscopic flaw related failure. From the data available, the loading arm length had no effect on σ_{3c}. The inner radius was not expected to have a significant effect on σ_{3c}, but this conclusion could not be confirmed because of differences in laminate quality for each curve geometry. The thicker specimens had the lowest value of σ_{3c} because of poor laminate quality. Width was found to affect the value of σ_{3c} only slightly. The wider specimens generally had a slightly lower strength since more material was under high stress and, hence, had a larger probability of containing a significant flaw.

Introduction

Because of low interlaminar strengths of laminated composites, interlaminar failures can be a predominant failure mode. Interlaminar failure may be predicted using strain energy release rate and interlaminar fracture toughness data if stress singularities are present, or, if the stresses are finite, stress and interlaminar strength data may be used. In the latter case, transverse width strength, σ_{2c}, determined from flat 90° specimens is often used to represent interlaminar tension strength, σ_{3c}. However, if the actual interlaminar tension strength is significantly different than the transverse width strength, predictions will be incorrect. Consequently, a method is needed to measure the interlaminar tension strength.

Several attempts have been made to design an interlaminar tension strength specimen. In Ref. 1, sixteen unidirectional specimens of 24 plies each were adhesively bonded together to create a 384-ply bonded laminate. A radius was machined into the specimen to give a minimum area in the center. Aluminum shanks were also bonded to the ends so that a tension load could be applied. For an XAS/914C carbon/epoxy specimen, an average σ_{3c} of 75.0 MPa was measured. This compared with an average σ_{2c} of 83.0 MPa determined from flat 90° specimens. However, failure in the interlaminar tension specimens was often close to a bond line. In Ref. 2, a similar method was attempted using thick (50 and 100 plies) unidirectional and cross-ply laminates. A radius was machined into the specimens to give a minimum area at the center, and aluminum shanks were bonded to the ends for load application. For an AS4/3501-6 carbon/epoxy specimen, an average σ_{3c} of 43.0 MPa was measured. This compared to an average σ_{2c} value of 57.6 MPa from flat $[90]_{100}$ specimens. However, the manufacture of thick laminates and the machining were considered by the authors to be disadvantages to this type of specimen.

In Ref. 3, unidirectional curved laminates were used to determine σ_{3c} data for AS4/3501-6. The curved laminates were essentially "L" shaped with the interlaminar tension failure occurring around the angle. A special loading fixture had to be manufactured to apply a load normal to the loading arm to open the specimen. An average σ_{3c} of 45.0 MPa was measured with this type of specimen. This compared to an average σ_{2c} value of 65.4 MPa obtained from $[90]_{24}$ flat laminates. In Ref. 4, a semi-circular curved beam specimen was used to determine σ_{3c} of G40-600/5245C carbon/epoxy. These laminates were of poor quality and had a high void content and variations in thickness. The data from the semicircular beam were grouped into two sets: one with an average σ_{3c} of 58.0 MPa and the other with an average strength of 32.5 MPa. The weaker data set was considered to be a flaw related failure whereas the stronger data set was proposed to be a true material property. Also in Ref. 4, an elliptical curved beam specimen was used to determine σ_{3c} of T300/934 carbon/epoxy. The manufacturing method was improved, and a very high quality part was

produced with no discernable flaws. For these specimens, a mean strength of 107.1 MPa was measured which was almost twice the in-plane transverse strength. A review of curved beam testing and interlaminar tensile failure was given in Ref. 5.

This paper describes an alternate configuration of the curved beam specimen which offers many advantages over the other methods for determining the interlaminar tension strength. The specimen geometry is much easier to manufacture than the other specimens. The geometry resembles many parts currently being used on actual aircraft such as webs and spars. Also, the test can be performed in a simple tensile testing machine without a special loading fixture. The test section of the curved beam is more representative of a composite structure than a flat tensile coupon and, hence, may give more representative strengths to use in failure predictions.

Specimen Configuration and Test Procedure

The curved beam specimen is shown schematically in Fig. 1. Various widths w, thicknesses t, inner radii r_i and loading arm lengths L were used as shown in Table 1. The material used was AS4/3501-6 carbon/epoxy. The material properties were taken from Ref. 3 and were:

$$E_\theta = 140\,\text{GPa}, \quad E_r = 11.0\,\text{GPa}, \quad G_{r\theta} = 5.84\,\text{GPa}, \quad \nu_{r\theta} = 0.0237$$

where the subscript θ coincides with the fiber direction. The laminates were laid up in 300 mm wide strips over the corner of a solid aluminum block. The corner of the block had the appropriate radius to form the inner radius indicated in Table 1. Each of the straight arms was 80 mm long. All the laminates were unidirectional with the fibers running in the direction shown in Fig. 1. The laminates were unidirectional to prevent matrix cracks and edge stresses from initiating delaminations [3]. The laminates were cured in an autoclave according to the material manufacturer's instructions. A thermal blanket was also used on the 48-ply specimens to

3

ensure uniform heating. The specimens were then machined to the specified width from the 300 mm panel. The exact width and thickness of each specimen were then measured with a vernier caliper. All specimens were dried prior to testing using the following cycle: 1 hour at 95°C, 1 hour at 110°C, 16 hours at 125°C, and 1 hour at 150°C.

Initially, loads were applied via aluminum hinges clamped to the loading arms. Adhesively bonding the hinges to the surface was attempted, but the adhesive bond invariably failed prior to interlaminar tension failure. In some configurations of the beam, the failure loads were sufficiently high to bend or even break the aluminum hinges. Hence, a steel loading fixture was manufactured to replace the hinges and is shown in Figs. 1 and 2. The method of load application is also included in Table 1. This loading mechanism allowed the specimen to be tested in a standard tension testing machine without the requirement of a special loading fixture such as used in Ref. 3. A screw-driven machine was used with the displacement controlled at 0.5 mm/min. Loads and displacements were digitally recorded and the initial interlaminar tension failure was generally recorded as a sudden decrease in load. To ease the observation of the location of interlaminar tension failure the sides of the specimen were painted white with a water based typewriter correction fluid.

Analysis

To determine the stresses throughout the cross section, Lekhnitskii solutions for a curved beam with an end load and for a curved beam with a moment were used [6]. Corrections were made to the Lekhnitskii solution to produce a solution for a pure end load. Corrections were also made to the applied moment to account for reductions in moment arm length. An elementary beam theory solution and a NASTRAN finite element analysis were also used to compare with the Lekhnitskii solution.

Lekhnitskii Solution

Lekhnitskii developed two sets of equations for the stresses in a curved beam segment with cylindrical anisotropy [6]. A set of equations was developed for a curved beam with an end load and for a curved beam with a moment at each end. The stresses caused by the loading shown in Fig. 1 were calculated by superimposing the stresses from Lekhnitskii's two solutions (Fig. 3). However, the stress distribution applied to the curved segment in Lekhnitskii's end load solution produced an end moment resultant as well as an end force resultant. Consequently, corrections were made to the end load solution by using Lekhnitskii's moment solution to subtract out the stresses caused by this additional moment (Fig. 3). Ref. 6 did not indicate that an end moment resultant was produced by the loading. Appendix A contains the stress equations for the two Lekhnitskii solutions and the modifications to the end load solution.

Because Lekhnitskii's solutions were for a curved beam segment only, the force applied to the loading arm was translated to the end of the curved segment as a moment and a force (Fig. 3). The stress equations are very sensitive to small changes in the moment arm length. Consequently, corrections were developed to obtain a more accurate moment arm length [Appendix B]. Corrections were calculated to include the offset of the loading pin from the neutral axis ($\Delta + t/2$, see Fig. 1) and the shortening of the moment arm caused by the rotation and displacement of the end of the beam prior to failure. The correction due to the loading pin offset was determined to be the only significant effect relative to the experimental error and was the only correction included in the final moment calculation. This correction reduced the moment arm length by up to 30% in some configurations. Corrections due to the rotation and displacement of the end of the beam were a maximum 4.1%. This correction was greatest in the thin specimens.

The radial stress, including corrections, at any location is given by Eq. 1. The derivation is contained in Appendices A and B.

5

$$\sigma_r = \frac{P}{rwg_1}\left[\left(\frac{r}{r_o}\right)^\beta + \rho^\beta\left(\frac{r_o}{r}\right)^\beta - 1 - \rho^\beta\right]\sin(\theta+\omega)$$

$$-\frac{P\left(L\cos(\omega) - \frac{1}{2}(r_i+r_o)\sin(\omega) - \left(\Delta+\frac{t}{2}\right)\sin(\omega)\right)}{r_o^2 wg}\left[1 - \frac{1-\rho^{\kappa+1}}{1-\rho^{2\kappa}}\left(\frac{r}{r_o}\right)^{\kappa-1} - \frac{1-\rho^{\kappa-1}}{1-\rho^{2\kappa}}\rho^{\kappa+1}\left(\frac{r_o}{r}\right)^{\kappa+1}\right] \tag{1}$$

The analysis assumed a state of plane strain. However, the stresses calculated by assuming a state of plane stress or plane strain were almost identical. The variables in eq. (1) are defined in the appendices. The geometry variables are also shown in Fig. 1. The expressions for the tangential stresses and shear stresses are given in Appendix B. For the loading arrangement shown in Fig. 1, ω is equal to 45°, and Eq. 1 reaches a maximum for any value of radius, r, at θ equals 45°. To determine the location, r, where σ_r is a maximum, Eq. 1 may be differentiated with respect to r and equated to zero or may be determined by incrementally increasing r. The latter technique was employed in this study.

Elementary Beam Theory

An elementary beam theory method to determine the maximum radial stress was proposed in Ref. 5 as

$$(\sigma_r)_{max} = \frac{3P\left(L\cos(\omega) - \left(\Delta+\frac{t}{2}\right)\sin(\omega)\right)}{2wt(r_i r_o)^{1/2}} \tag{2}$$

The variables are defined the same as those used in Eq (1). This expression accounts for the maximum stress location being at a position other than the center thickness and may be used as an approximation of the maximum radial stress.

Finite Element Analysis

An MSC/NASTRAN finite element analysis was conducted on the specimen to determine the stress distribution. By using symmetry, only half of the specimen was modeled (one loading arm and half of the curved region). The force was applied to the straight loading

arm so that a comparison could be made with the Lekhnitskii solution to determine if the translation of the loading force to the end of the curved segment affected the stresses in the region of interest ($\theta = 45°$). Four-noded quadrilateral elements were used with 24 elements in the thickness direction and one element for every degree in the circumferential direction. A transition was made to a coarser mesh to model the straight loading arm. For convenience, the force was applied at the neutral axis so a loading pin height correction was not necessary. The effects of geometric nonlinearities and large displacements were not modelled.

Analytical Results

The radial and tangential stress distributions, σ_r and σ_θ, in the thickness direction are shown for a 3.0 mm thick curved laminate with an inner radius of 5.0 mm at $\theta = 45°$ and a moment arm length, L, of 25 mm in Fig. 4. The shear stresses are zero at $\theta = 45°$ and are an order of magnitude smaller than the radial stress for other values of θ. Hence, the shear stresses may be considered negligible. The radial stress increases from zero at the free surface and reaches a maximum prior to the center of the specimen. The tangential stress was a maximum at the free surfaces and varied from tension to compression as r was increased. In the region where the radial stress is a maximum, the tangential stress is of the same magnitude. Since the strength in the circumferential direction (fiber direction) is typically two orders of magnitude higher than in the radial direction, a failure at this location was attributed to radial stress alone.

For comparison, the stress results from the finite element analysis and from the modified Lekhnitskii solution are both shown in Fig. 4. The maximum stress predicted by beam theory (Eq. 2) is also shown. There were no differences between the stress predictions from the finite element analysis and the Lekhnitskii solution. Consequently, the translation of forces in the Lekhnitskii solution were assumed not to have affected the stresses in the region of interest ($\theta = 45°$). An analysis of a similar configuration indicated that the

7

stresses were affected by the loading method only within a region that was within 15° of the ends of the curved segment [3]. The beam theory prediction was approximately 8% lower than the maximum stress predicted by the other two methods and, hence, would give conservative values of σ_{3c}.

The distribution of radial stress, σ_r, and tangential stress, σ_θ, through the thickness for beams of three different thicknesses is plotted at $\theta = 45°$ in Fig. 5. All the beams had an inner radius of 5.0 mm and a loading arm length of 25 mm. The loads were applied at the neutral axis of the loading arm, and small corrections to the moment arm were not included. For a given force, the thicker beams had a lower value of maximum radial stress than the thinner beams. Also, the location of the maximum radial stress moved away from the center and closer to the inner radius as thickness was increased. The maximum tangential stress was lower for thicker beams, and the location where $\sigma_\theta = 0$ did not change significantly with thickness. Also, for the thicker 48-ply specimens, the curve is flatter near the region of maximum radial stress than for the thinner specimens. Consequently, a larger percentage of the cross-sectional area is under high stress for the thicker specimens.

The location of the maximum radial stress with various thicknesses and inner radii is given as a carpet plot in Fig. 6. Again, the loads were considered to be applied at the neutral axis of the loading arm, and small corrections to the moment arm were not included. As the inner radius increased, the maximum radial stress decreased, and the location of maximum radial stress moved towards the center of the thickness. Additionally, as the laminate thickness increased, the maximum radial stress decreased, and the location moved away from the center of the thickness towards the inner radius.

Experimental Results

Load-Displacement Curves

A plot of a typical load-displacement curve for each curve geometry is given in Fig. 7. In all five of these curves, both the loading arm and width of the specimen are equal to

8

25.4 mm. The 16-ply specimens had an almost linear load-displacement relationship to failure with a slight increase in stiffness with increasing loads. This stiffness increase was probably caused by a slight decrease in the length of the moment arm because of a deflection of the loading arm. For the 24-ply laminates with a 3.2- or an 8.5-mm radius, the load-displacement curves were also nearly linear. For the 24-ply specimens with the 5.0-mm radius, the stiffness was greatly reduced relative to the other 24-ply specimens since the load was applied using hinges rather than the steel fixture as indicated in Table 1. These hinges were thin aluminum and would bend on loading which produced a nonlinear load-displacement curve. The increased compliance and nonlinearity of this configuration should not affect the strength calculation since the displacements were small. The 48-ply specimens were loaded using the steel loading mechanism and were very stiff. Consequently, the load-displacement relationship was nonlinear because of the small displacements relative to the compliance of the machine and loading fixture. The machine and fixture compliance was measured and found to have a similar nonlinear behavior of the same magnitude.

In many of the specimens, subcritical damage developed before failure occurred where the specimen had a significant loss of load and stiffness. The strength was calculated based on the load corresponding to this initial damage if subcritical damage developed prior to failure. The development of subcritical damage caused small load drops which resulted in steps in the loading curves. More of the wider specimens had these steps than the narrower specimens. An example of a stepped loading curve is shown in Fig. 7 for the 24-ply specimen with the 3.2-mm radius. The cause for these steps is discussed below. The 16-ply specimens did not have any steps before a sudden failure occurred which resulted in an approximately 80% drop in load. For the 24-ply specimens with a radius of 3.2 mm, half of the 25.4-mm wide specimens had steps while none of the 12.7-mm wide specimens had steps. For the 24-ply 8.5-mm radius specimens, only one of the 25.4 mm wide specimens had steps in the loading curve, and none of the 12.7-mm wide specimens had load drops. When the 24-ply specimens failed, the load dropped approximately 50% from the maximum. In general, the

load dropped a greater percentage for specimens that failed at higher loads. The 48-ply specimens were unloaded at the first sign of damage as indicated by a small load drop (approximately 70 N) and circumferential crack. These damaged specimens were later reloaded until a large drop in load occurred. Most of the load curves had several more steps before a final failure occurred. The final failure occurred at load that was more than twice the value at which initial damage developed. At failure, the load would typically drop by 40%.

After failure, circumferential cracks in the curved segment were observed on the edges of all specimens. These cracks extended slightly into the loading arm. Fig. 8 shows an example of a circumferential crack for a 24-ply specimen with an inner radius of 8.5-mm. The 16-ply specimens tended to have the most cracks with approximately seven cracks per side. Most specimens, however, had one to three cracks on each side. These cracks were rarely in the same radial location on opposite sides of the same specimen. The small load steps that occurred prior to failure resulted in a small circumferential crack on one or both edges. For the 48-ply specimens, the cracks formed by the load steps always formed near mid thickness.

Failure Strengths

The interlaminar strength, σ_{3c}, was calculated for each specimen using the modified Lekhnitskii solution (Eq. 1) and the load at which initial damage was detected. The strengths along with the mean and coefficient of variation are given in Table 2. Figure 9 shows the individual strength measurement for each of the test specimens. The strengths were expected to be approximately equal for each data set. However, the data sets generally fell into a high or a low category of strength. The eight sets of data that fell into the low strength category were composed of all the 48-ply specimens and the 24-ply specimens with inner radii of 8.5 mm and 5.0 mm. The high strength set consisted of the 16-ply specimens and the 12.7-mm wide 24-ply specimens with the 3.2 mm radius. The 24-ply 25.4-mm-wide specimens with the 3.2 mm radius had the most scatter with strengths that fell into both categories. However, a significant amount of scatter occurred within each data set. For each

10

curve configuration, the effect of different width specimens was small. However, four of the five curve geometries showed a slight decrease in strength for the wider specimens. The strength was not significantly affected by the two loading arm lengths, L, used in this study.

Since small sample sizes were used to measure the interlaminar strength, an estimation of experimental uncertainty was performed [7]. Many of the variables, such as the modulus in the radial direction, are not known with a high degree of accuracy. Consequently, it was desirable to know which measurements were most crucial to the accuracy of the interlaminar strength prediction. The details of this analysis are given in Appendix C. For the case of an inner radius of 5.0 mm with a loading arm length of 25.4 mm and a width of 25.4 mm, the percent uncertainty ranged from 6 6 % in the 48-ply specimens to 14.0% in the 16-ply specimens The two variables that contributed the most to the overall uncertainty were the thickness and the loading arm length. The analysis was also fairly sensitive to the value of the inner radius. The overall uncertainty was rather insensitive to material properties. A large estimated uncertainty of 30% in the radial modulus, E_r, resulted in less than a 1.3% uncertainty in the predicted value of radial stress. Consequently, the uncertainty in the material properties did not affect the overall accuracy of the prediction.

Fracture Patterns

Several specimens of each configuration were cut perpendicular to the fiber direction at $\theta = 45°$ using a low-speed diamond saw. The cut surfaces were then examined under a microscope to observe the fracture pattern across the width of the specimen. The observations from the cut surfaces are listed below. In addition, the fiber volume fraction was observed to vary through the thickness. This variation was quantified by measuring the ply thickness variation across the thickness using a microscope. The average ply thickness in a small region was determined by dividing a known distance (0.824 mm) by the number of plies contained in that distance. The results of these measurements are shown in Fig. 10. In general, the quality of the laminates was highest in the inner half of the thickness which

11

corresponded to the region with the smallest ply thicknesses. In most laminates, the ply thicknesses increased steadily from the inner radius to the outer radius.

The 16-ply specimens with an inner radius of 5.0 mm had the highest average value of interlaminar strength (Fig. 9). These laminates also appeared to be of the best quality. The cross sections were not observed to contain large resin pockets or voids like many of the other configurations. Also, the ply thickness did not change significantly across the thickness of the specimen (Fig. 10). The resin rich regions between the plies were observed to be very small. The average ply thickness at $\theta = 45°$ was 0.123 mm which was the lowest of all the specimen configurations. The fracture pattern consisted of numerous cracks scattered across the entire cross section (Fig. 11). Most cracks were translaminar and discontinuous with many branches which gave the fracture pattern a "shattered" appearance. The cracking appeared to be more extensive in the higher strength specimens than in the lower strength specimens. There was no significant difference between the failure patterns in the different width specimens.

The 24-ply specimens with an inner radius of 3.2 mm also had a high average strength (Fig. 9). These laminates had more than a 40% increase in ply thickness from the inner to the outer radius. Consequently, there were large resin-rich layers between the plies toward the outer radius. However, no large voids were observed. The failure pattern for the 25.4-mm wide specimens consisted of several long cracks on the outer half of the thickness which tended to be predominantly interlaminar. On the inner half, the cracks were more translaminar with many branches which were similar to the cracks in the 16-ply specimens but not nearly as dense. No specific region existed where the cracks were more concentrated. A lower and a higher strength 12.7-mm wide specimen were examined and found to contain fewer cracks than the 25.4-mm wide specimens. The higher strength specimen contained two interlaminar cracks (interfaces of plies 7/8 and 11/12 from inner radius) that were connected by a translaminar crack to create a crack that spanned the entire width (Fig. 12). The lower strength

specimen contained a single crack (interface of 12/13 from inner radius) near the edge which was connected to two cracks that ran two-thirds of the way across the width of the specimen.

The set of 24-ply specimens which had an inner radius of 5.0 mm had an interlaminar strength that fell in the lower group (Fig. 9). These specimens were also used to determine the effects of a change in moment arm length on the interlaminar strength. The ply thicknesses increased approximately 20% from the inner radius to the outer radius (Fig. 10). On the outer half of the thickness, a large resin-rich layer was observed between every group of four plies. These large resin-rich layers may have developed during the manufacturing process where the laminate was debulked every four plies. The failure in all of the specimens occurred primarily on a single interface in the resin-rich layer between plies 8 and 9 from the outer surface (Fig. 13). The low strengths may have resulted because of the failure at this manufacturing defect. No difference in the failure pattern was observed for the different moment arm lengths or specimen widths.

The 24-ply specimens with an inner radius of 8.5 mm had low strength values (Fig. 9). These specimens also had the highest average ply thickness (0.152 mm) in the curved region of any of the configurations. The laminate thickness around the radius increased by as much as 25% going from the edge to the center of the arc which resulted in a significantly higher resin content than the other 24-ply specimens. In addition, many small voids and resin pockets were observed across the cut section. The fiber volume fraction also varied across the thickness with the thickest plies and largest resin-rich regions in an area two-thirds of the way from the inner radius. Many interlaminar and translaminar cracks were observed throughout the two 25.4-mm wide specimens that were examined. The stronger of these two specimens had more extensive cracking, and the largest cracks were located approximately 45% of the way through the thickness. The weaker specimen had more voids and resin-rich regions and did not have a predominant cracking path across the width. In addition to these cracks, both specimens had large translaminar cracks that ran through the resin-rich region in the outer half of the thickness. The strongest of the 12.7-mm wide specimens was also sectioned and

13

examined. This specimen failed primarily on a single interface between plies 6 and 7 from the inner radius and had no cracking in the upper half of the specimen.

The 48-ply specimens had the lowest values of interlaminar strength and the least strength variability (Fig. 9). The area closest to the outer radius was observed to contain several large voids as well as large resin pockets. The ply thickness increased 18% from the inner radius to the outer radius (Fig 10). The resin rich regions between the plies were much larger near the outer radius than near the inner radius. The individual plies could be easily distinguished across the entire section without polishing the surface. During loading, as mentioned above, all of these specimens had many small subcritical failures which were detected audibly and by a small drop in the load. Two specimens (12.7- and 25.4-mm wide) were sectioned after the first sub-critical failure was detected. In both specimens, three small cracks were observed between the ply interfaces in the mid-section, and it was these cracks that caused the small load drop. The photomicrograph of the 25.4-mm wide section is shown in Fig. 14a. This interlaminar cracking occurred primarily at the interface between plies 26 and 27 (from the inner radius) in the 12.7-mm wide specimen and between plies 28 and 29 in the 25.4-mm specimen. On further loading, the cracks would accumulate and finally coalesce as shown by a section of a different specimen loaded to failure (Fig. 14b). When the cracks coalesce, a more significant load drop occurred. Two specimens of each width were sectioned following final failure. The greatest concentration of cracks was located in the inner half of the radius. This region contained numerous branching translaminar cracks. The cracks in the outer half of the radius were primarily interlaminar. Several cracks were also observed emanating from large voids (Fig. 14b).

Discussion

Unlike the transverse tension specimen discussed in Ref. 8, the interlaminar tension specimen is not stressed uniformly. The maximum radial stress occurs at a single point

14

through the thickness and around the curved portion. However, the maximum stress does have a constant value at any point across the width. Therefore, any reduction of width should reduce the probability of large flaws in that section and give higher strengths. In general, the mean σ_{3c} values of the wider specimens were similar or slightly lower than the narrower specimens indicating a small effect of width on σ_{3c}. Also, the strength measurements were not affected significantly by the two loading arm lengths, L, used in this study.

Since the effect of width and loading arm length were considered insignificant relative to the scatter, a mean σ_{3c} was calculated for all specimens with the same curve geometry and plotted as bars in Fig. 15. The two data sets for the 24-ply specimens with an inner radius of 3.2 mm were not combined since several of the 25.4-mm wide specimens had different failure modes due to the development of subcritical damage prior to failure. The range of scatter is also shown for all the data sets. A large range of interlaminar strengths was obtained for the five curve geometries. The differences in the mean values of interlaminar strength are indicative of laminate quality rather than geometry effects. For thicker laminates, a larger volume is under high stress, and the probability of large flaws being present is increased. Therefore, if all the laminates were of equal quality with an equal distribution of flaws, the thicker laminates should have a lower value of σ_{3c}. However, the effect of thickness cannot be readily compared in the experimental results since laminate quality was inversely proportional to thickness. Consequently, the trend of decreasing strengths with increasing thicknesses must be attributed to laminate quality which resulted in different failure mechanisms. The best quality of laminate was produced for the thinnest specimens (16-ply), and these had the highest strengths. The 48-ply laminates were of the poorest quality and had the lowest strength. All of the 48-ply specimens had large voids and resin pockets in the curved region which were visible to the naked eye. The 24-ply specimens had a quality in between that of the 16- and 48-ply laminates. The 24-ply specimens with the 5.0-mm radius all failed at the same ply interface because of a manufacturing defect.

15

The best indicator of strength for a given laminate was the local ply thicknesses. The highest strength configurations had the lowest ply thicknesses in the inner half of the thickness which also corresponds to the region of highest radial stress. In general, the quality of the laminate decreased from the inner radius to the outer radius. In Ref 4, a similar result occurred when significantly higher values of σ_{3c} were obtained for laminates where high compaction pressure was used in manufacturing curved specimens. The quality of the laminates could not be determined using C-scans since ultrasonic equipment could not be used in highly curved regions. Manufacturing defects were most likely the initiation sites for much of the damage. The strength appeared to be extremely sensitive to flaws. The strength of the lower strength specimens was probably controlled by larger macroscopic defects such as voids. These type of defects may have been detected by ultrasonic methods if ultrasonic equipment could be used in highly curved regions. For specimens with higher strengths, the strength may have been a function of smaller microscopic flaws such as fiber/matrix debonds.

Strength results from several other studies were also plotted in Fig. 15 for comparison. The mean value of σ_{3c} determined from flatwise tension tests [2] fell between the lower and higher strength groups. The mean value of σ_{3c} determined from "L" shaped curved laminates [3] also fell within a similar range. However, the quality of the laminates used in these two studies was not known since no sectioning was done. Several values of σ_{2c} [2,3,8] are also shown in Fig. 15. These values of σ_{2c} were higher than the σ_{3c} values measured in the other studies [2,3] and in the low strength group of this study. However, these values of σ_{2c} are still significantly less than the values of σ_{3c} measured in the higher strength group in this study. This result is consistent with the results of Ref. 4. The average value of σ_{3c} determined from curved elliptical specimens made of T300/934 carbon/epoxy was almost twice the reported value of σ_{2c} [9] determined from transverse tensile tests. The curved elliptical specimen was manufactured using very high compaction pressure which produced a very high quality specimen. T300/934 has very similar properties to the AS4/3501-6 used in the current study.

A Weibull statistical analysis [11] was conducted on a group of higher strength data sets and on a group of lower strength data sets [Appendix D]. The high strength values of σ_{3c} relative to the reported values of σ_{2c} can be accounted for in terms of volumetric scaling. The transverse tensile tests involve a uniform stress over a large volume of material while the interlaminar tensile tests with curved beams have a nonuniform stress applied over a very small volume. In Ref. 8, Weibull scaling laws were used to scale data from transverse tensile tests to specimens where only a small volume of material was under high stress. The results from Ref. 8 indicate that Weibull scaling laws can accurately predict the difference in strength of transverse tension coupons and the σ_{3c} values of the "good" quality curved beams tested in this study.

Strength data obtained from curved beam test specimens are very relevant to the design process. The curved beam is a more representative specimen than a flat laminate to determine failure or delamination in a composite structure of complex shape. Specimens with curved geometries present unique manufacturing problems that do not occur in flat panels. Consequently, failure modes and strengths obtained from curved beam specimens will closely resemble those in the actual structure since the test specimen will have similar manufacturing defects. Because of the curved nature of the specimen, it is not possible to use conventional C-scan methods to determine specimen quality. Hence, the only means of determining specimen quality is by testing and, as in this work, obtaining sets of data representing "good" specimens and "bad" specimens. Similarly, in complex composite structures, quality cannot be determined using conventional C-scans. Hence, all the data from the curved beam specimen, including the "bad" specimen data, may be useful in predicting failure in a structure.

In this study, interlaminar tension strengths were highly dependent on the manufacturing quality of the specimens. This is a severe problem since the quality of highly curved parts cannot be routinely determined using conventional C-scans. Also, a high quality specimen was difficult to manufacture. However, several alternatives are available to improve the

17

through-the-thickness strength of curved composite structures. The manufacturing process can be improved to consistently obtain a better quality part. Also, ultrasonic methods can be improved to determine laminate quality in highly curved regions. A tougher matrix may be used to reduce the flaw sensitivity that a laminate with a brittle matrix has. A material system with *through-the-thickness reinforcement* such as textile preforms also may be used. If through-the-thickness reinforcement is used, the strength should be much greater than traditional laminates and less dependent on the manufacturing process.

Concluding Remarks

A curved beam, loaded so that the radius of curvature increases, produces an interlaminar tension stress that is zero at the free surfaces and reaches a maximum at some location through the thickness. The tangential stress is tensile at the inside radius and compressive at the outside radius and small where the radial stress is a maximum. Therefore, if a unidirectional specimen is used with the fiber direction in the tangential stress direction, interlaminar tension failure will occur. This paper describes one configuration in which to test the curved beam as a method to determine interlaminar strength, σ_{3c}. The curved beam is a more representative specimen than a flat laminate to determine failure or delamination in a composite structure of complex shape since curved geometries present unique manufacturing problems that do not occur in flat panels. The specimen contains a 90° bend with straight arms extending from this curved portion. A hinged loading mechanism was attached to the arms and then pulled in tension until interlaminar tension failure occurred. Geometry effects of the specimen were studied; namely the effects of loading arm length, inner radius, thickness, and width. The specimens generally did not fail along a single interface but developed many interlaminar and translaminar cracks. The average strength from each configuration fell into either a high or a low strength category. In the lower strength category, failure may have occurred because of large macroscopic flaws such as voids or resin pockets which were observed in

18

failed specimens. In the higher strength category, the failure was probably caused by smaller microscopic flaws such as fiber/matrix debonds. The σ_{3c} values determined from the high strength data sets was significantly higher than the reported values of σ_{2c} from transverse tensile tests. This relative increase in strength can be accounted for by using volumetric scaling laws. From the data available, the loading arm length had little effect on σ_{3c}. Width was found to only have a slight effect on σ_{3c}. The wider specimens had slightly lower strengths because more material is under high stress and the specimen, therefore, has a larger probability of containing a flaw. The effects of thickness and inner radius could not be determined because of the large variation of laminate quality between specimens of different curve geometries. The specimen geometries with the higher strengths tended to have lower ply thicknesses in the inner half of the thickness which corresponds to the region of highest stress.

Appendix A - Lekhnitskii Solution

Lekhnitskii [6] developed a solution for the stresses in a curved beam with cylindrical anisotropy for two different loading cases: a curved beam under pure bending and a curved beam with an end force.

Case I - Curved beam under pure bending (plane-stress)

$$\sigma_r^m = -\frac{M}{r_o^2 wg}\left[1 - \frac{1-\rho^{\kappa+1}}{1-\rho^{2\kappa}}\left(\frac{r}{r_o}\right)^{\kappa-1} - \frac{1-\rho^{\kappa-1}}{1-\rho^{2\kappa}}\rho^{\kappa+1}\left(\frac{r_o}{r}\right)^{\kappa+1}\right] \tag{A1}$$

$$\sigma_\theta^m = -\frac{M}{r_o^2 wg}\left[1 - \frac{1-\rho^{\kappa+1}}{1-\rho^{2\kappa}}\kappa\left(\frac{r}{r_o}\right)^{\kappa-1} + \frac{1-\rho^{\kappa-1}}{1-\rho^{2\kappa}}\kappa\rho^{\kappa+1}\left(\frac{r_o}{r}\right)^{\kappa+1}\right] \tag{A2}$$

$$\tau_{r\theta}^m = 0 \tag{A3}$$

where

$$g = \frac{1-\rho^2}{2} - \frac{\kappa}{\kappa+1}\frac{(1-\rho^{\kappa+1})^2}{1-\rho^{2\kappa}} + \frac{\kappa\rho^2}{\kappa-1}\frac{(1-\rho^{\kappa-1})^2}{1-\rho^{2\kappa}} \tag{A4}$$

$$\kappa = \sqrt{\frac{E_\theta}{E_r}} \tag{A5}$$

$$\rho = \frac{r_i}{r_o} \tag{A6}$$

Case II - Curved beam loaded by an end force (plane-stress)

$$\sigma_r = \frac{P}{rwg_1}\left[\left(\frac{r}{r_o}\right)^\beta + \rho^\beta\left(\frac{r_o}{r}\right)^\beta - 1 - \rho^\beta\right]\sin(\theta+\omega) \tag{A7}$$

$$\sigma_\theta = \frac{P}{rwg_1}\left[(1+\beta)\left(\frac{r}{r_o}\right)^\beta + (1-\beta)\left(\frac{r_o}{r}\right)^\beta\rho^\beta - 1 - \rho^\beta\right]\sin(\theta+\omega) \tag{A8}$$

$$\tau_{r\theta} = \frac{P}{rwg_1}\left[\left(\frac{r}{r_o}\right)^\beta + \rho^\beta\left(\frac{r_o}{r}\right)^\beta - 1 - \rho^\beta\right]\cos(\theta+\omega) \tag{A9}$$

where

$$\beta = \sqrt{1 + \frac{E_\theta}{E_r}(1 - 2v_{r\theta}) + \frac{E_\theta}{G_{r\theta}}}$$

(A10)

$$g_1 = \frac{2}{\beta}(1 - \rho^\beta) + (1 + \rho^\beta)\ln(\rho)$$

(A11)

The analysis was converted to plane strain by replacing E_r, E_θ, and $v_{r\theta}$ in Eqs. A5, A10, and A11 by $\dfrac{E_r}{1 - v_{zr}v_{rz}}$, $\dfrac{E_\theta}{1 - v_{z\theta}v_{\theta z}}$, and $\dfrac{v_{r\theta}}{1 - v_{zr}v_{rz}}(1 + \dfrac{v_{z\theta}v_{rz}}{v_{r\theta}})$, respectively.

The symbols are defined as:

cf	Subscript denoting modified stress equation for an end force
E_r	Modulus in the radial direction
E_θ	Modulus in the tangential direction
f	Subscript denoting stress induced by an end force (Case II)
$G_{r\theta}$	Shear modulus
m	Subscript denoting stress induced by a moment (Case I)
M	Applied moment
P	End force
r,θ	Cylindrical coordinates of any point in the curved segment
r_i	Inner radius of curved segment
r_o	Outer radius of curved segment
w	Width of the specimen
σ_r, σ_θ, $\tau_{r\theta}$	Stress components in curved segment
v	Poisson's ratio
ω	Angle of the load relative to the face of the loaded end of the curved segment

Dimensions and variables are illustrated in Fig. 1.

Correction to Lekhnitskii's End Force Solution

The stress distribution applied to the end of the curved segment results in an end force resultant and an end moment resultant. Consequently, it was necessary to derive a correction to Lekhnitskii's end force solution to subtract out the additional moment. This correction is shown schematically in Fig. 3. This correction is not necessary when ω equals to zero as was the case in Ref. 3. This moment per unit width (M^*) applied to the end of the curved segment was calculated by integrating, along the face of the segment end, the product of the tangential stress component, σ_θ, and the distance from the neutral axis.

$$M^* = \int_{r_i}^{r_o} \sigma_\theta {}_{(\theta\,=\,0)} \left(r - \frac{r_i + r_o}{2} \right) dr \approx \frac{P(r_i + r_o)}{2\,w} \sin(\omega) \tag{A12}$$

The actual stresses in a curved beam due to an end force resultant only were then calculated by subtracting the stresses caused by M^* from Lekhnitskii's original end force solution. Lekhnitskii's solution for a beam under pure bending was used to calculate the stresses due to M^*.

$$\sigma_r^f = \sigma_r^f - \sigma_r^m{}_{(M\,=\,M^*)} \tag{A13}$$

$$\sigma_\theta^f = \sigma_\theta^f - \sigma_\theta^m{}_{(M\,=\,M^*)} \tag{A14}$$

$$\tau_{r\theta}^f = \tau_{r\theta}^f \tag{A15}$$

Final Stress Equations for the Interlaminar Tension Strength Specimen

The stresses in the interlaminar tension strength specimen were calculated by superimposing the stresses from these two solutions (Eqs. A16-A18).

$$\sigma_r = \sigma_r^m + \sigma_r^f \tag{A16}$$

$$\sigma_\theta = \sigma_\theta^m + \sigma_\theta^f \tag{A17}$$

$$\tau_{r\theta} = \tau_{r\theta}^m + \tau_{r\theta}^f \tag{A18}$$

22

Appendix B - Corrections to the Applied Moment

The stress analysis was very sensitive to the changes in the length of the moment arm. An error in the moment arm length translates directly into the same percentage error in the stress calculation. Consequently, it was important to calculate the exact length of the moment arm at failure. Therefore, several corrections were considered for inclusion in the basic moment calculation. These corrections included the offset of the loading pin from the neutral axis and the shortening of the moment arm caused by the rotation and displacement of the end of the beam on loading.

The basic moment was simply calculated as the force, P, multiplied by the length, L, of the moment arm (B1)

$$M^{basic} = P\,L\,\sin(45) \tag{B1}$$

Prior to loading, the moment arm length was reduced by the offset of the loading fixture from the neutral axis of the laminate (Fig. 1). This correction was calculated as

$$M^{hinge} = -P\left(\Delta + \frac{t}{2}\right)\sin(45) \tag{B2}$$

where Δ is the height of the hinge from the surface of the specimen, and t is the specimen thickness. This was the most significant correction to the basic moment calculation. Omitting this correction resulted in an error up to 30% in some cases. This correction was more significant in the thicker specimens

The next most significant correction was in accounting for the deflection of the end of the loading arm at failure. Simple beam theory was used to calculate the deflection caused by the transverse component of the load and caused by the moment created by the loading point offset from the neutral axis. A geometric nonlinear interaction exists between the tension load and the transverse load. This interaction was accounted for using tabulated reaction coefficients [10]. The tension load had a negligible effect on the deflection

23

calculated from the moment and transverse load only. The deflection correction was the most significant for the 16-ply specimens where an average 4.1% error would result if the deflection was not accounted for. However, the error was reduced for thicker specimens since the moment of inertia increases proportionally to the cube of the thickness. The average error for the 24-ply specimens was 2.5%, and the error was less than 1% for the 48-ply specimens. These errors were considered insignificant relative to the experimental error [Appendix C] and were not taken into account in the final stress equation. The nonlinear effect of shortening due to beam rotation was also calculated. This effect was most significant in the 16-ply specimens, but made less than a 0.2% in the overall moment calculation. Consequently, the effect of shortening was also neglected.

The final moment equation (B3) that was used was simply the basic moment plus the correction for the hinge offset .

$$M^{total} = M^{basic} + M^{hinge} = P\left(L - \Delta - \frac{t}{2}\right)\sin(45)$$

(B3)

The effect of end displacement and rotation only becomes significant for very thin specimens with high loads and does not generally need to be included.

Final Stress Equations for the Interlaminar Tension Strength Specimen

Eq. B3 was substituted into Eqs. A16-A18 to obtain the final equation for the stresses in the interlaminar tension strength specimen. The final equations (B4-B6) are shown below.

$$\sigma_r = \frac{P}{rwg_1}\left[\left(\frac{r}{r_o}\right)^\beta + \rho^\beta\left(\frac{r_o}{r}\right)^\beta - 1 - \rho^\beta\right]\sin(\theta + \omega)$$

(B4)

$$- \frac{P\left(L\cos(\omega) - \frac{1}{2}(r_i + r_o)\sin(\omega) - \left(\Delta + \frac{t}{2}\right)\sin(\omega)\right)}{r_o^2 wg}\left[1 - \frac{1 - \rho^{\kappa+1}}{1 - \rho^{2\kappa}}\left(\frac{r}{r_o}\right)^{\kappa-1} - \frac{1 - \rho^{\kappa-1}}{1 - \rho^{2\kappa}}\rho^{\kappa+1}\left(\frac{r_o}{r}\right)^{\kappa+1}\right]$$

24

$$\sigma_\theta = \frac{P}{rwg_1}\left[(1 + \beta)\left(\frac{r}{r_0}\right)^\beta + (1 - \beta)\left(\frac{r_0}{r}\right)^\beta \rho^\beta - 1 - \rho^\beta\right]\sin(\theta + \omega)$$

$$\text{(B5)}$$

$$-\frac{P\left(L\cos(\omega) - \frac{1}{2}(r_1 + r_0)\sin(\omega) - \left(\Delta + \frac{t}{2}\right)\sin(\omega)\right)}{r_0^2 wg}\left[1 - \frac{1 - \rho^{\kappa+1}}{1 - \rho^{2\kappa}}\kappa\left(\frac{r}{r_0}\right)^{\kappa-1} + \frac{1 - \rho^{\kappa-1}}{1 - \rho^{2\kappa}}\kappa\rho^{\kappa+1}\left(\frac{r_0}{r}\right)^{\kappa+1}\right]$$

$$\tau_{r\theta} = \frac{P}{rwg_1}\left[\left(\frac{r}{r_0}\right)^\beta + \rho^\beta\left(\frac{r_0}{r}\right)^\beta - 1 - \rho^\beta\right]\cos(\theta + \omega)$$

$$\text{(B6)}$$

Appendix C - Sensitivity Study

An estimation of experimental uncertainty was performed to determine which measurements were most crucial to the accuracy of the interlaminar strength prediction. The estimation method consisted of first estimating the uncertainty of each variable and then applying a relationship that specifies how the uncertainty of individual variables propagates into the overall uncertainty in the prediction [7].

The uncertainty in each variable was estimated as shown in Table C1.

TABLE C1--Estimation of experimental uncertainties

No.(i)	Variable (v_i)	Uncertainty (u_i)	Percent error for individual variables		
			16 ply	24-ply	48 ply
1	E_r	± 30 %	0.0	0.6	1.3
2	E_θ	± 10 %	0.1	0.2	0.5
3	$G_{r\theta}$	± 20 %	0.1	0.2	0.5
4	$v_{r\theta}$	± 20 %	0.0	0.0	0.0
5	L	± 1.00 mm	3.8	4.2	4.7
6	P	± 1 % (load cell)	1.0	1.0	1.0
7	r_i	± 0.20 mm	3.1	2.8	2.3
8	t	± 0.20 mm	13.1	7.6	4.1
9	w	± 0.05 mm	0.2	0.2	0.2
		maximum σ_r, MPa	87.2	35.1	17.1
		overall uncertainty (U)	±12.2	±3.2	±1.2
		(percent uncertainty)	(14.0%)	(9.2%)	(6.9%)

26

The overall uncertainty, U, was calculated as

$$U = \left[\sum_{i=1}^{n} \delta_i^2 \right]^{1/2}$$

(C1)

where i is the variable number, n is the number of variables, and δ_i is the change in the overall prediction due to the uncertainty in variable i. The uncertainty caused by each variable, δ_i, was taken as the greater of

$$f(v_1,...,v_i+u_i,...,v_n) - f(v_1,...,v_i,...,v_n) \text{ or } f(v_1,...,v_i-u_i,...,v_n) - f(v_1,...,v_i,...,v_n)$$

$$\text{where } \sigma_r = f(v_1,...,v_n).$$

The modified Lekhnitskii solution was used for the experimental uncertainty analysis. The uncertainties in the test results are shown for three different thicknesses, t, for the case of an inner radius, r_i, of 5.0 mm, a loading arm length, L, of 25.4 mm, and a width, w, of 25.4 mm. The two variables that contribute the most to the overall uncertainty are the thickness and the loading arm length. For a constant value of the thickness measurement uncertainty, the overall uncertainty decreases with thickness. The overall uncertainty caused by the uncertainty in loading arm length decreased slightly with increasing thickness. The analysis was also fairly sensitive to the value of the inner radius, r_i. The overall uncertainty was rather insensitive to material properties. A large estimated uncertainty of 30 percent in the radial modulus, E_r, resulted in less than a 1.3 percent uncertainty in the predicted value of radial stress. When terms are added by the squares, only the larger terms contribute. Consequently, the uncertainty in the material properties did not affect the overall accuracy of the prediction.

27

Appendix D - Weibull Analysis

A Weibull statistical analysis was conducted on a group of higher strength data sets and a group of lower strength data sets. The data from the 16-ply specimens (both widths) were combined with that of the 24-ply specimens with an inner radius of 3.18 mm and a width of 12.7 mm to form a high strength group. A lower strength group was formed by combining the data sets from the 24-ply specimens with an inner radius of 5.0 mm. Data sets could be combined since the mean strengths varied only slightly between data sets (Table 2), and hence any volumetric effects on σ_{3c} between the specimen configurations were assumed to be small [8]. Also, the specimens from the data sets that were combined were of similar quality and had similar failure modes. The probability of failure at a given stress level, $P(\sigma)$, is given by

$$P(\sigma) = 1 - e^{-(\sigma/\sigma_c)^m} \tag{D1}$$

where m is the Weibull slope and σ_c is the characteristic strength [11]. The Weibull slope, m, characterizes the scatter and may be a constant for a given material system. A median ranking scheme was used to determine the probability of failure [8]. A value of m of 7.76 and a value of σ_c of 84.1 MPa were calculated for the high strength group. This value of m compares well with an m value of 7.68 obtained for 114 transverse tension tests of T300/5208 in Ref. 12. In general, a large number of tests are required to determined an accurate value of m [8]. For the low strength group, a value of m of 4.88 and a value of σ_c of 39.1 MPa were calculated. This smaller value of m indicates a larger amount of scatter. This value may be different from the other two values of m since the specimens from the lower strength group all failed at a macroscopic manufacturing defect rather than at a randomly distributed flaw in the microstructure of the material.

References

1. Martin, R.H. and Sage, G.N., "Prediction of the Fatigue Strength of Bonded Joints Between Multi-Directional Laminates of CFRP," Composite Structures, 6, 1986, pp. 141-163.

2. Lagace, P.A. and Weems, D.B., "A Through-the-Thickness Strength Specimen for Composites," Test Methods for Design Allowables for Fibrous Composites: 2nd Volume, ASTM STP 1003, C.C. Chamis, Ed., American Society for Testing and Materials, Philadelphia, 1989, pp. 197-207.

3. Martin, R.H. and Jackson, W.C., "Damage Prediction in Cross-Plied Curved Composite Laminates," presented at the Fourth ASTM Symposium on Composite Materials: Fatigue and Fracture, Indianapolis, Indiana, May 6-7, 1991. Also published as NASA TM 104089, July 1991.

4. Hiel, C.C., Sumich, M., and Chappell, D.P., "A Curved Beam Test Specimen for Determining the Interlaminar Strength of a Laminated Composite," Journal of Composite Materials, Vol. 25, July 1991, pp. 854-868.

5. Kedward, K.T., Wilson, R.S., and McLean, S.K., "Flexure of Simply Curved Composite Shapes," Composites, Vol. 20, No. 6, November 1989, pp. 527-536.

6. Lekhnitskii, S.G., "Anisotropic Plates," Gordon and Breach Science Publishers, New York, 1968, pp. 95-101.

7.   Kline, S. J. and McClintock, F. A., "Describing Uncertainties in Single-Sample Experiments," Mechanical Engineering, January 1953.

8.   O'Brien, T.K. and Salpekar, S.A., "Scale Effects on the Transverse Tensile Strength of Graphite Epoxy Composites," to be presented at the 11th ASTM Symposium on Composite Materials: Testing and Design, Pittsburgh, Pennsylvania, May 5-6, 1992.

9.   Wu, H.-Y. T. and Springer, G. S., "Impact Induced Stresses, Strains , and Delaminations in Composite Plates." Journal of Composite Materials, 1988, 22:533-560

10.   Roark, R. J. and Young, W. C., Formulas for Stress and Strain, Mc Graw-Hill, Inc., New York, 1975, pp. 147-152.

11.   Weibull, W., "A Statistical Theory of the Strength of Materials," Ing. Vetenskaps Akad. Handl., Royal Swedish Institute Engineering Research Proceedings, NR151, 1939.

12.   Rodini, B. T., and Eisenmann, J., "An Analytical and Experimental Investigation of Edge Delamination in Composite Laminates," Fibrous Composites in Structural Design, Planum Publishers, New York, 1980, pp. 441-457.

No. of Plies	Inner Radius, η (mm)	Thickness, t (mm)	Loading Arm Length, L (mm)	Nominal Width, w (mm)	No. of Specimens	Loading Mechanism
16	5.0	1.96	25.4	12.7	5	hinge
				25.4	6	fixture
24	3.2	3.35	25.4	12.7	6	fixture
				25.4	6	fixture
	5.0	3.36	25.4	12.7	5	hinge
				25.4	3	hinge
			50.8	12.7	5	hinge
				25.4	5	hinge
	8.5	3.66	25.4	12.7	6	fixture
				25.4	6	fixture
48	5.0	6.61	25.4	12.7	6	fixture
				25.4	6	fixture

Table 1. Test Matrix

No. of Plies	Inner Radius, η (mm)	Loading Arm Length, L (mm)	Nominal Width, w (mm)	Interlaminar Strength, σ_{3c} (MPa)	Mean	CV, %
16	5.0	25.4	12.7	92.9, 85.5, 66.7, 73.7, 88.2	81.4	13.3
			25.4	72.6, 77.6, 84.9, 88.1, 100.4, 62.7	81.1	16.2
24	3.2	25.4	12.7	89.4, 75.4, 88.1, 65.7, 66.0, 68.8	75.5	14.3
			25.4	18.0, 56.2, 76.4, 39.7, 40.8, 53.4	47.4	41.4
	5.0	25.4	12.7	25.6, 21.6, 32.3, 33.8, 36.6	30.0	20.7
			25.4	36.7, 37.7, 32.8	35.7	7.3
		50.8	12.7	37.4, 41.2, 34.0, 50.2, 22.3	37.0	27.5
			25.4	47.6, 34.2, 47.0, 35.7, 39.5	40.8	15.3
	8.5	25.4	12.7	48.7, 43.8, 49.9, 28.8, 44.6, 22.2	39.7	28.8
			25.4	15.9, 14.7, 29.9, 34.2, 47.8, 32.9	29.2	42.6
48	5.0	25.4	12.7	15.8, 16.8, 16.1, 16.4, 16.7, 18.5	16.7	5.5
			25.4	17.3, 15.6, 16.8, 16.9, 18.2, 17.7	17.1	5.3

Table 2. Interlaminar Tensile Strengths
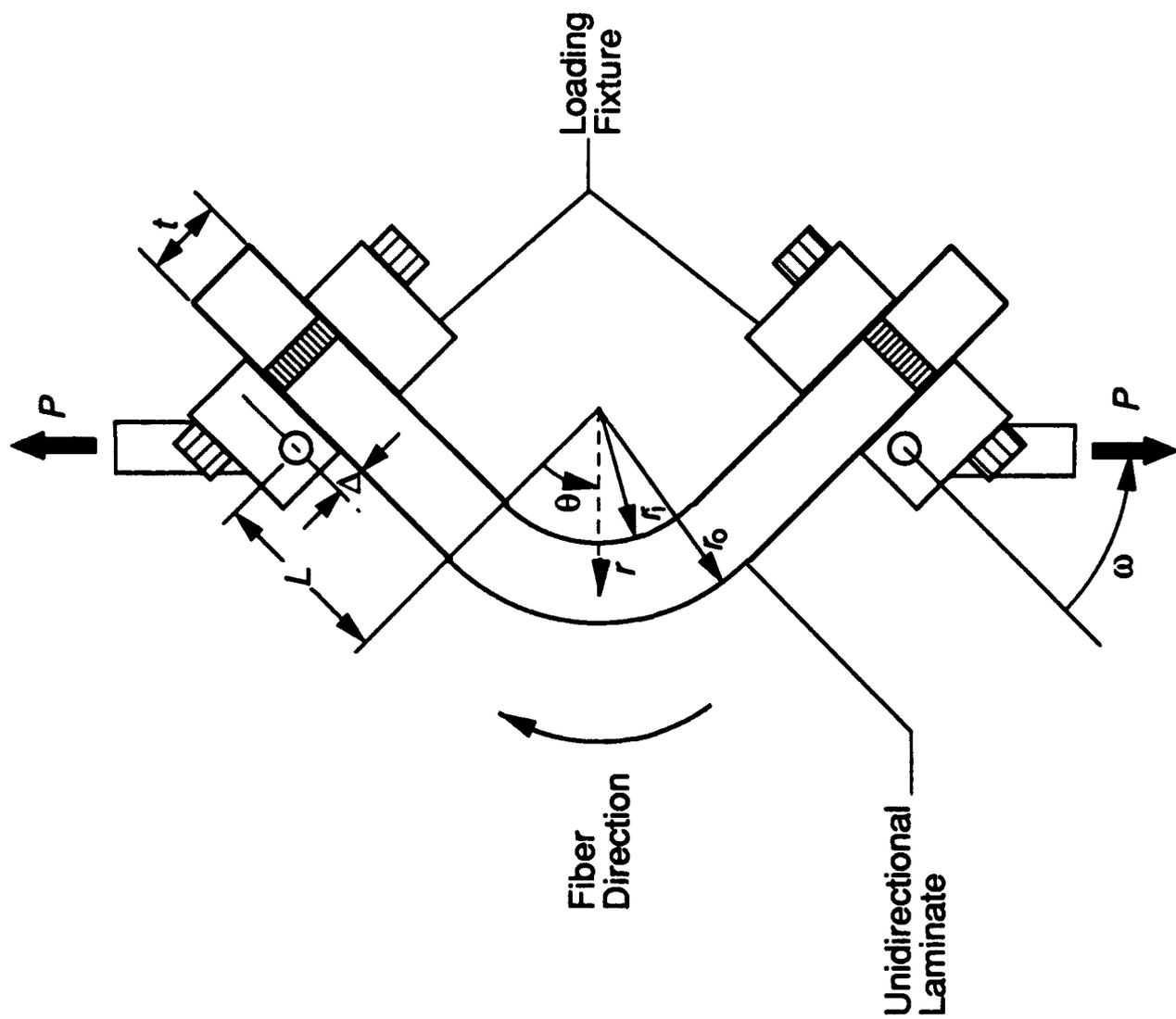
Fig. 1. - Schematic of interlaminar tension strength specimen

33
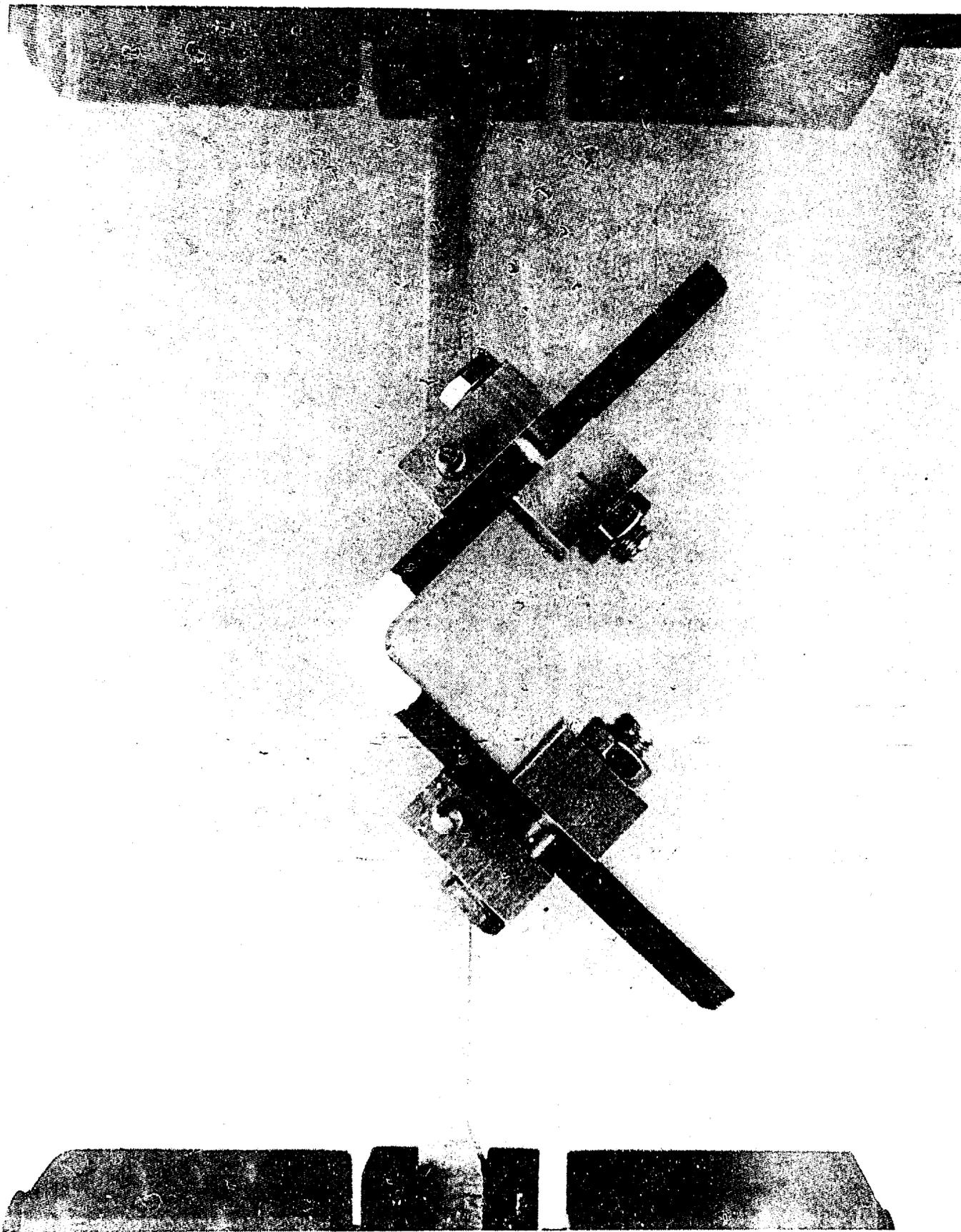
Fig. 2 - Photograph of interlaminar tension strength specimen and test fixture
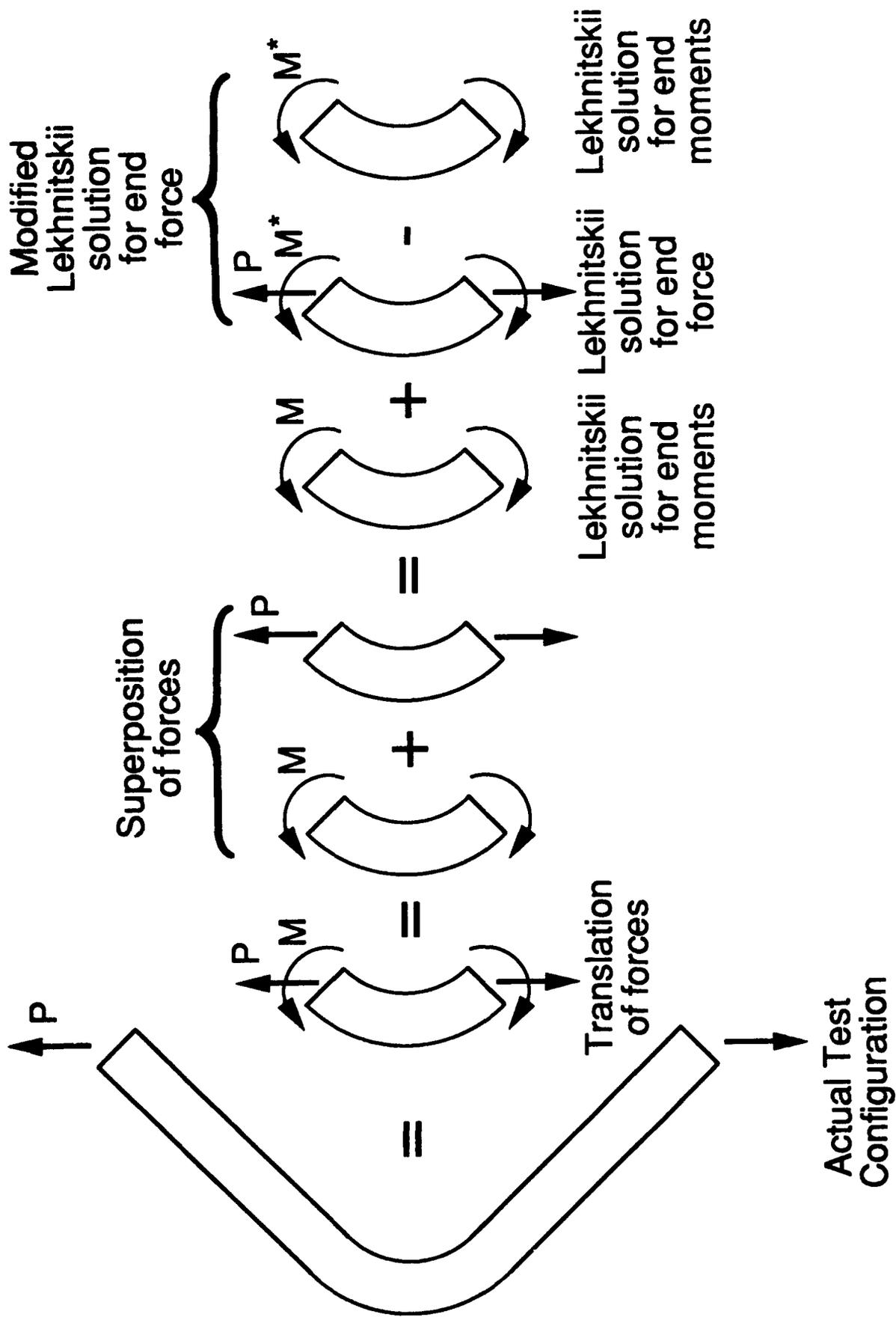
Fig. 3 - Superposition of Lekhnitskii solutions to obtain stresses for test configuration

35
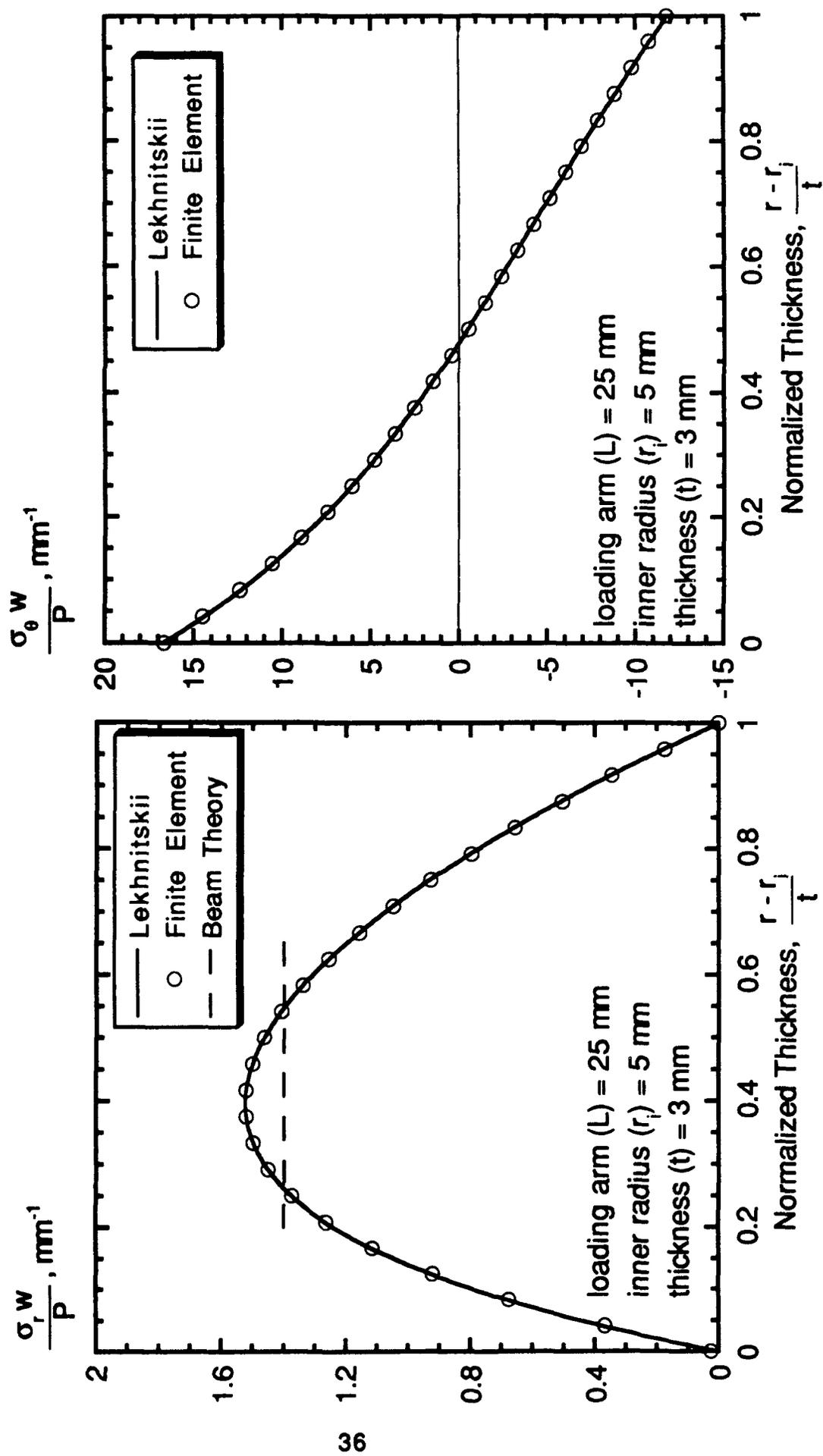
Fig. 4 - Comparison of analytical data reduction techniques

36
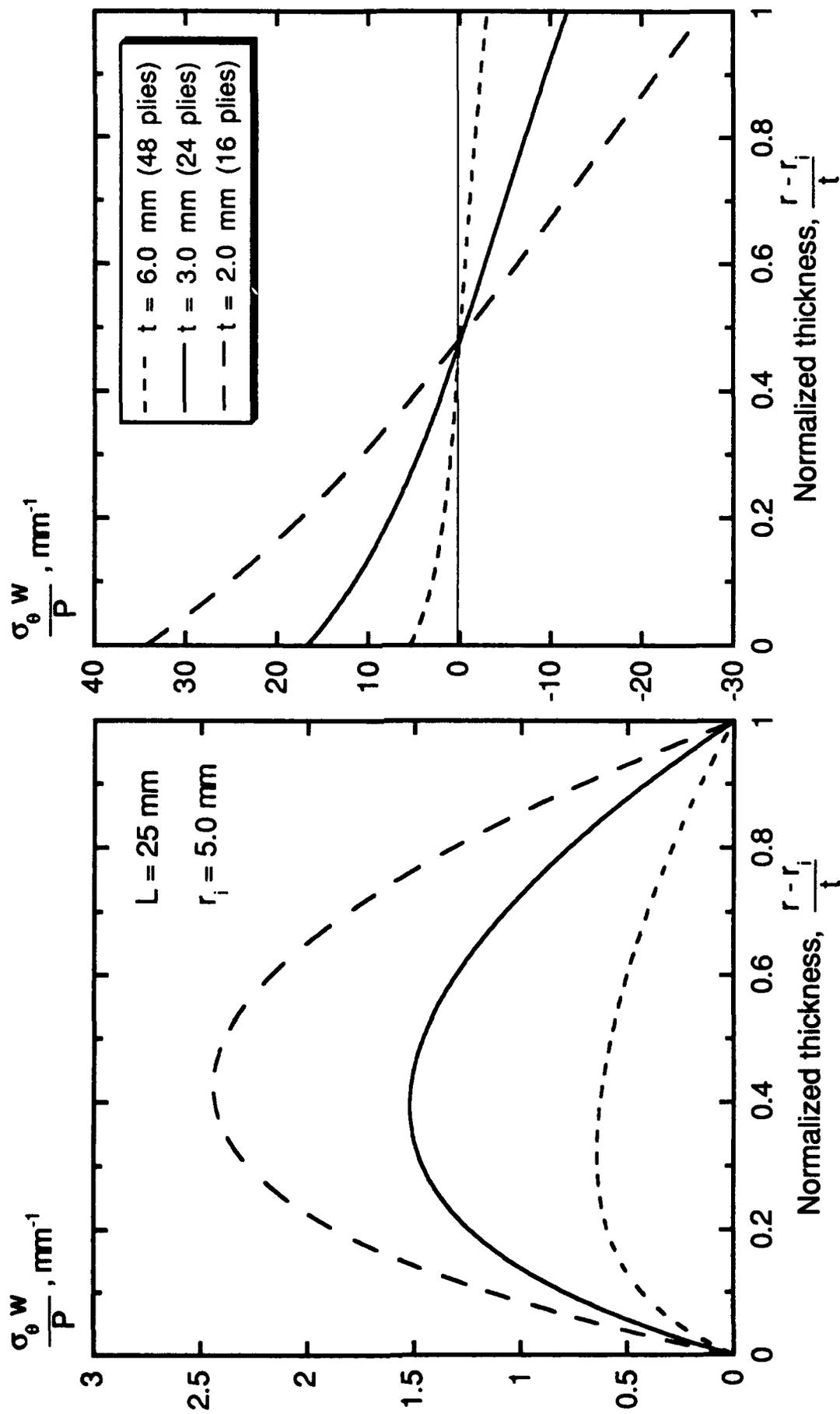
Fig. 5 - Effect of specimen thickness on stress distribution

37
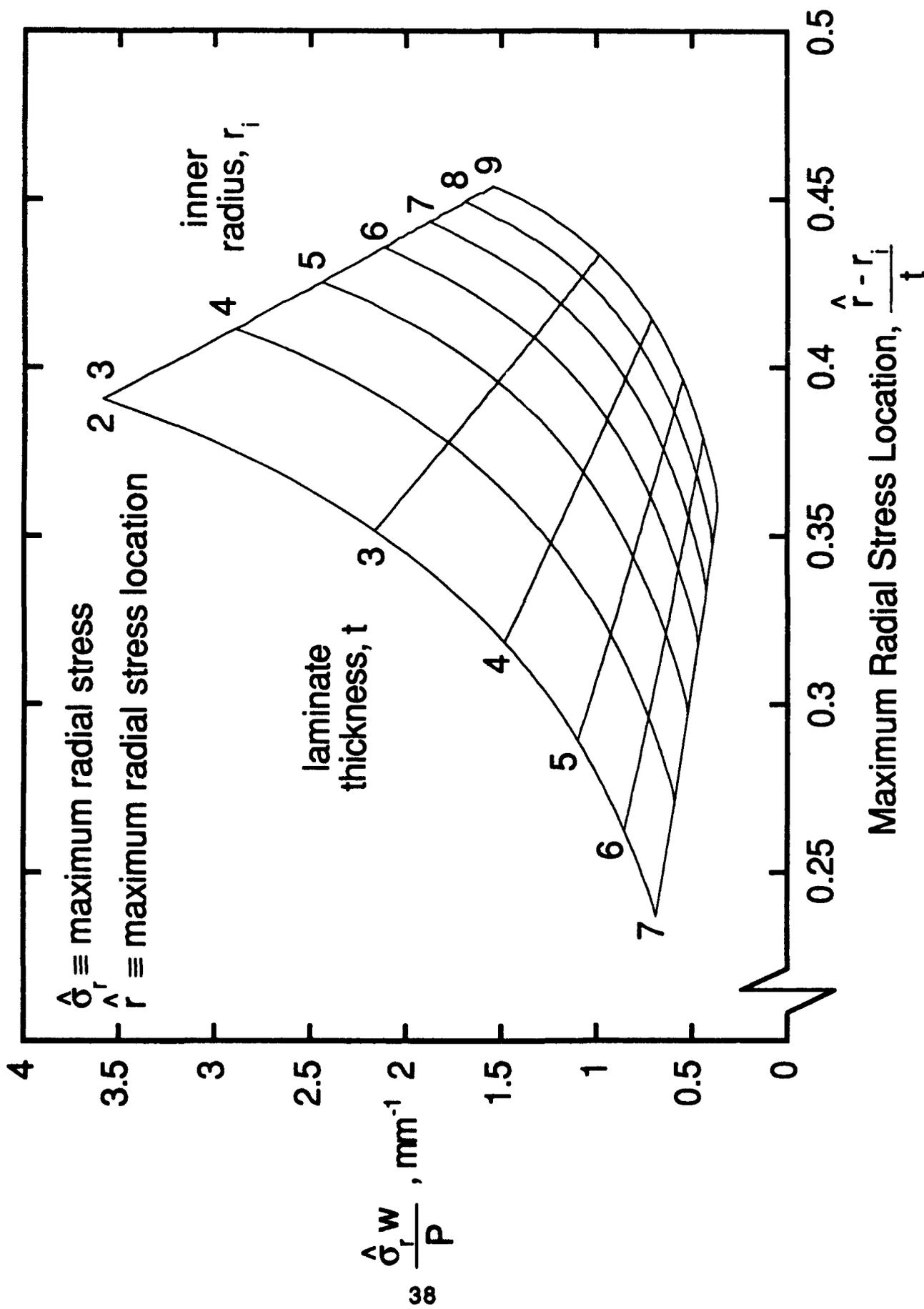
Fig. 6 - Location of maximum radial stress with different thicknesses and inner radii
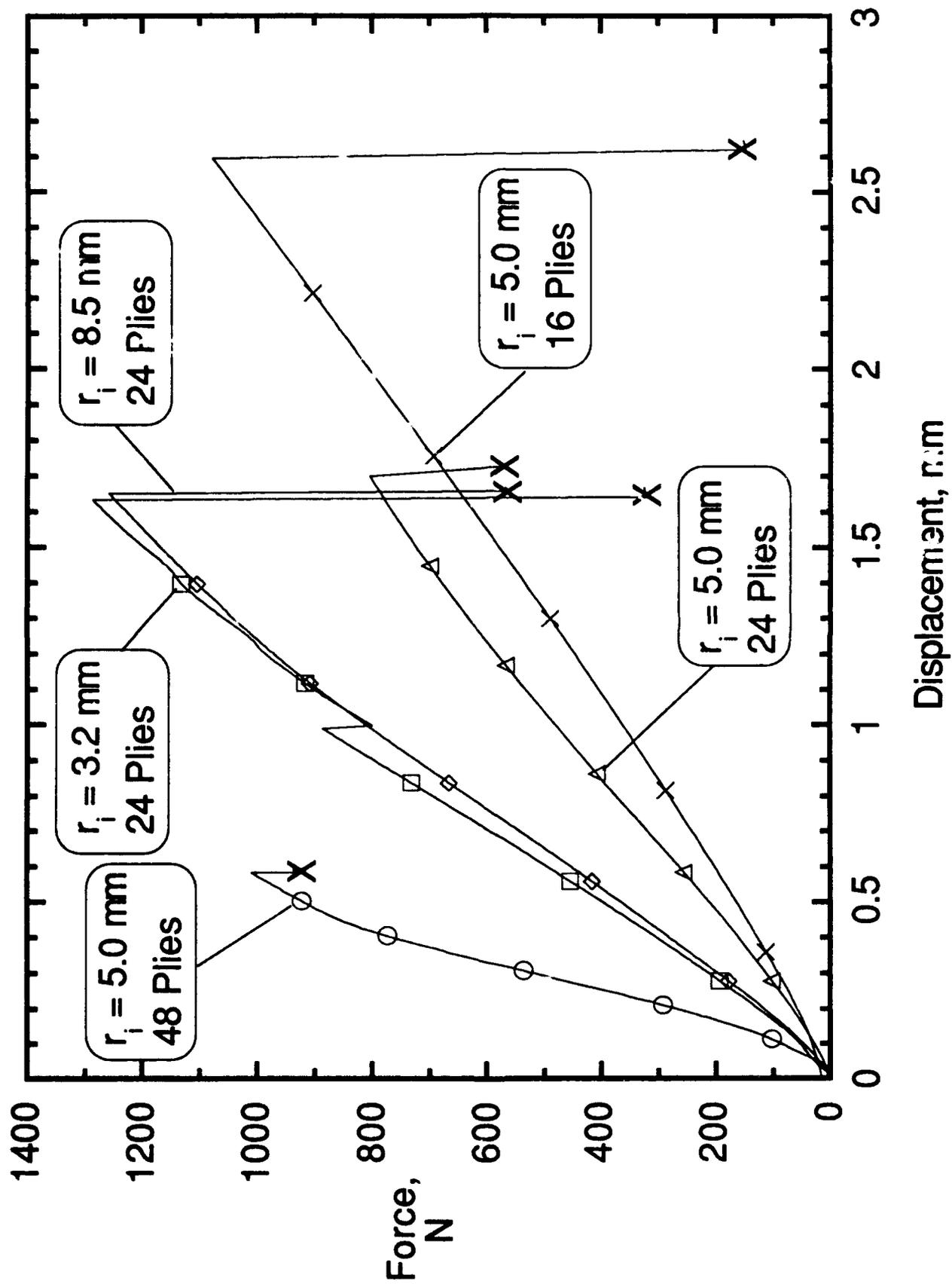
Fig. 7 - Typical load-displacement curves
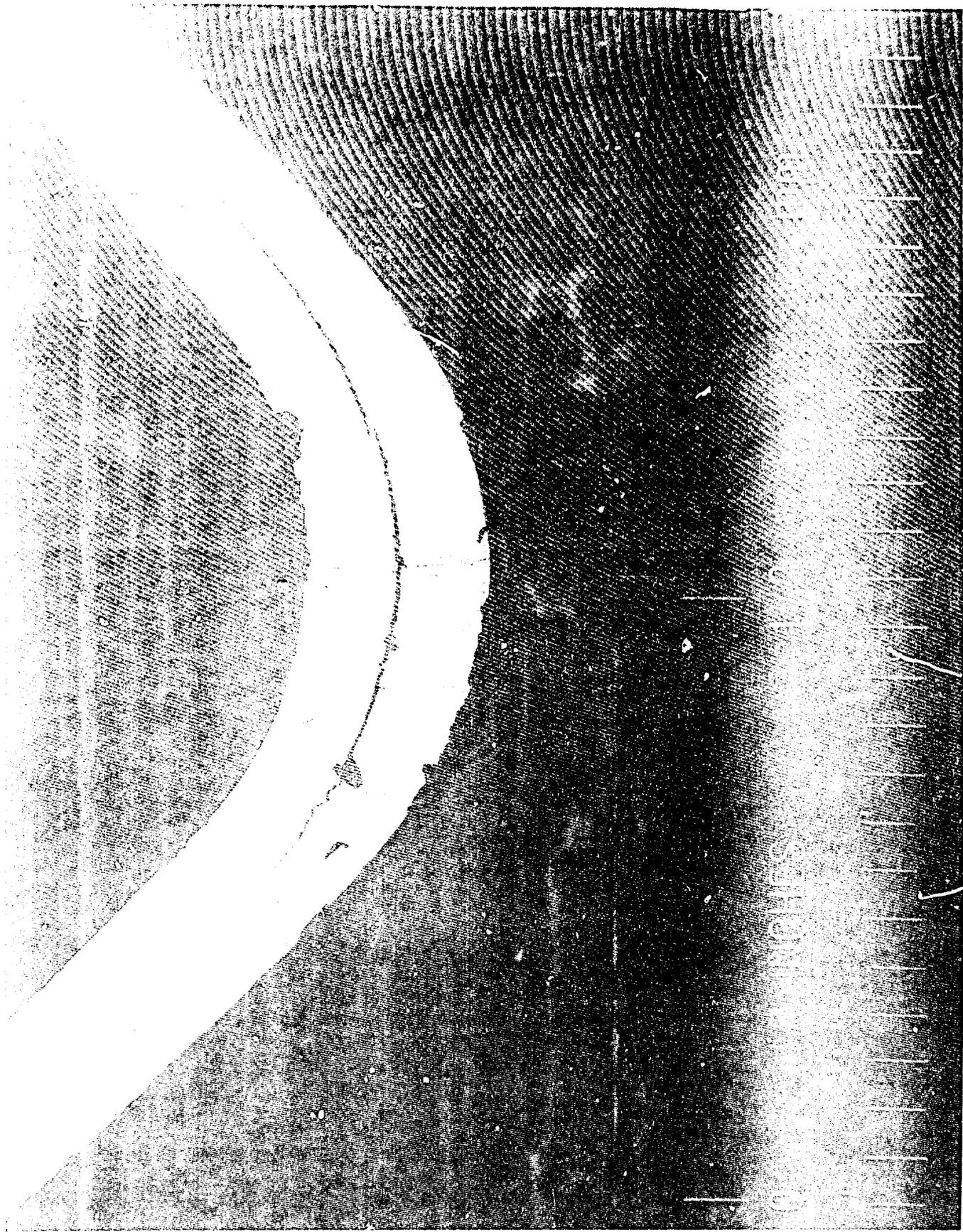
Fig. 8 - Circumferential crack on the edge of a 24-ply specimen with an $r_i = 8.5$ mm

40
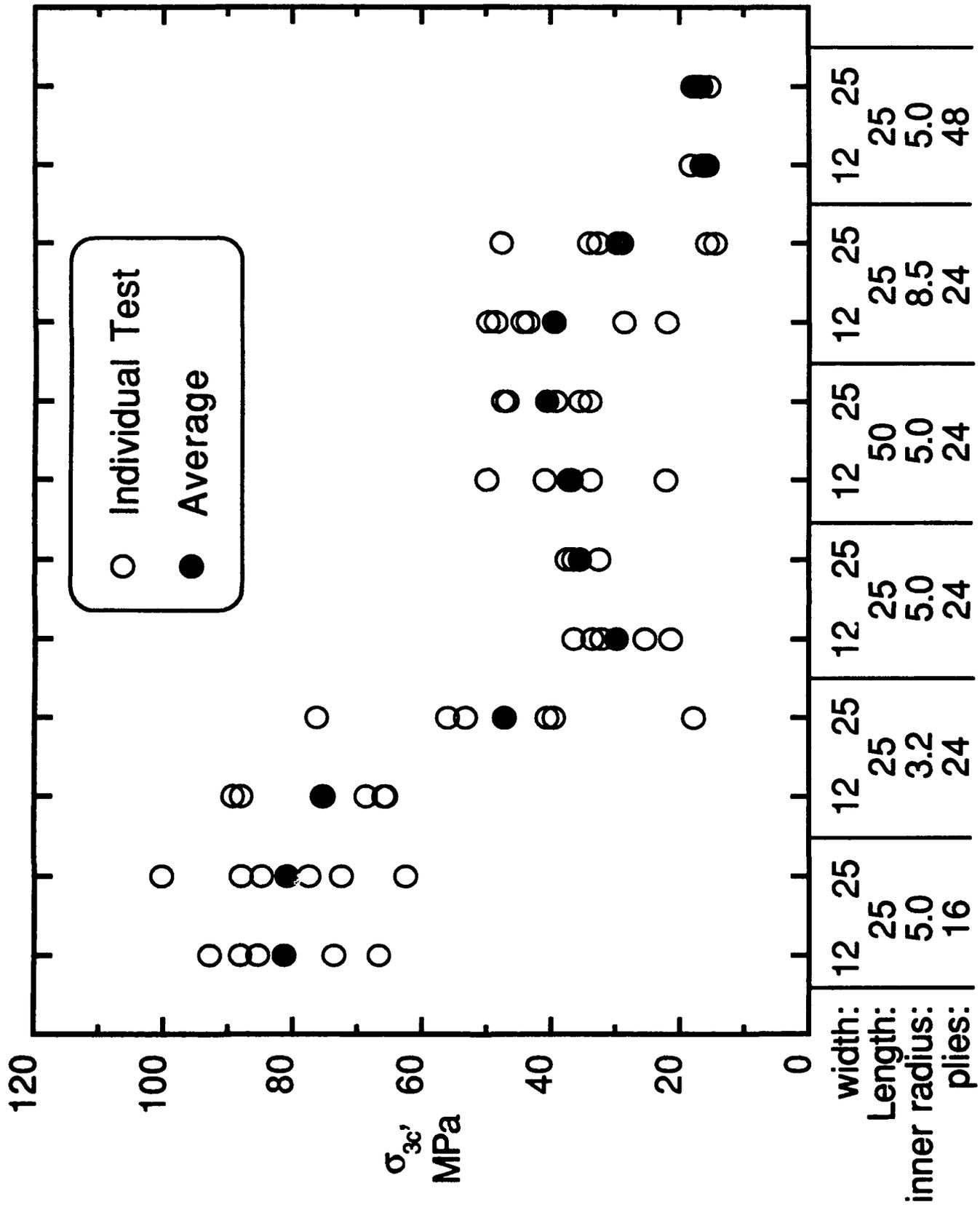
Fig. 9 - Experimental interlaminar tension strengths
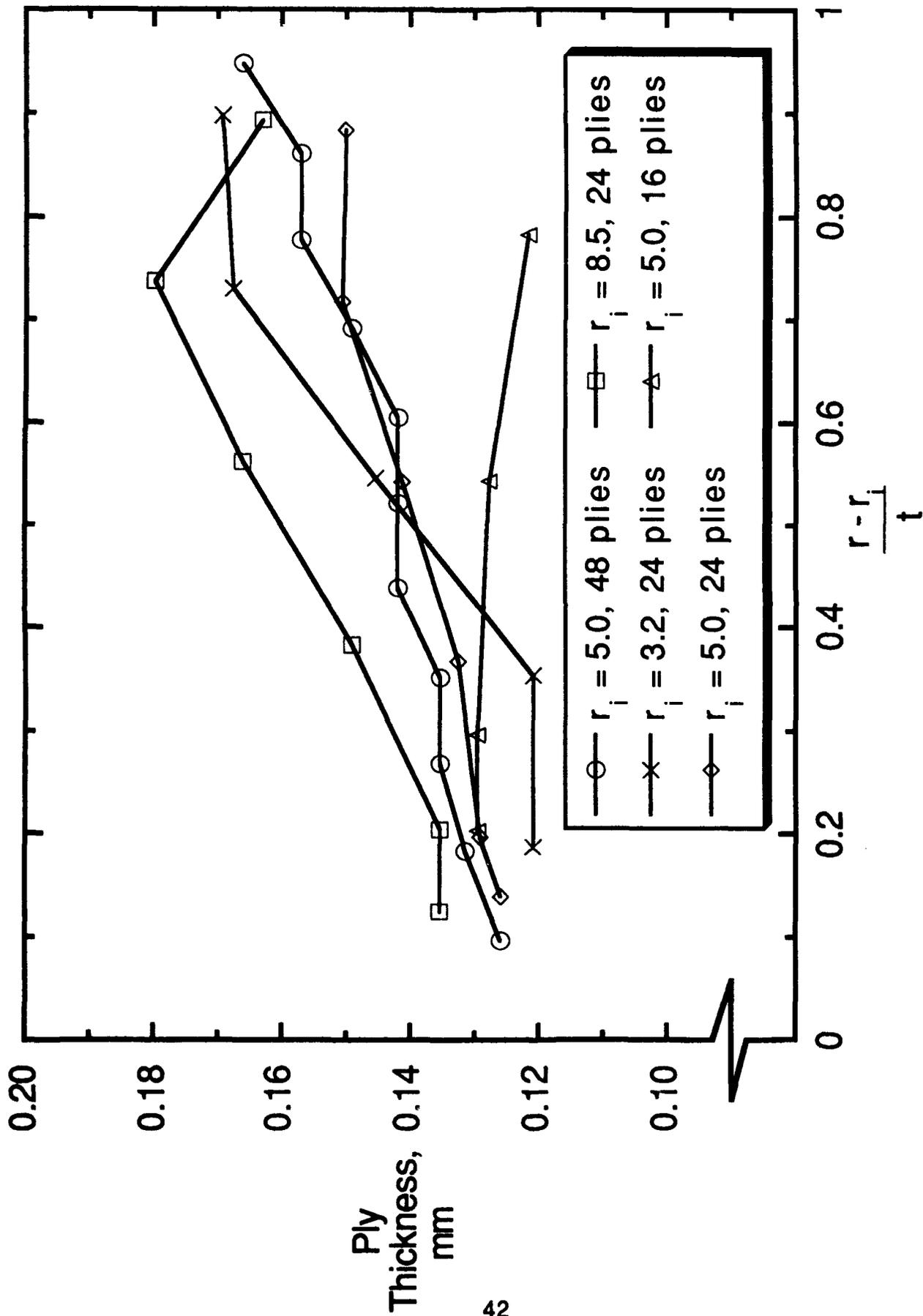
Fig. 10 - Variation of ply thickness through the thickness

- $r_i = 5.0$, 48 plies
- $r_i = 3.2$, 24 plies
- $r_i = 5.0$, 24 plies
- $r_i = 8.5$, 24 plies
- $r_i = 5.0$, 16 plies

The x-axis is labeled $\dfrac{r - r_i}{t}$ with values 0, 0.2, 0.4, 0.6, 0.8, 1.

The y-axis is labeled "Ply Thickness, mm" with values 0.10, 0.12, 0.14, 0.16, 0.18, 0.20.

outer radius

inner radius

0   1   2   3 mm
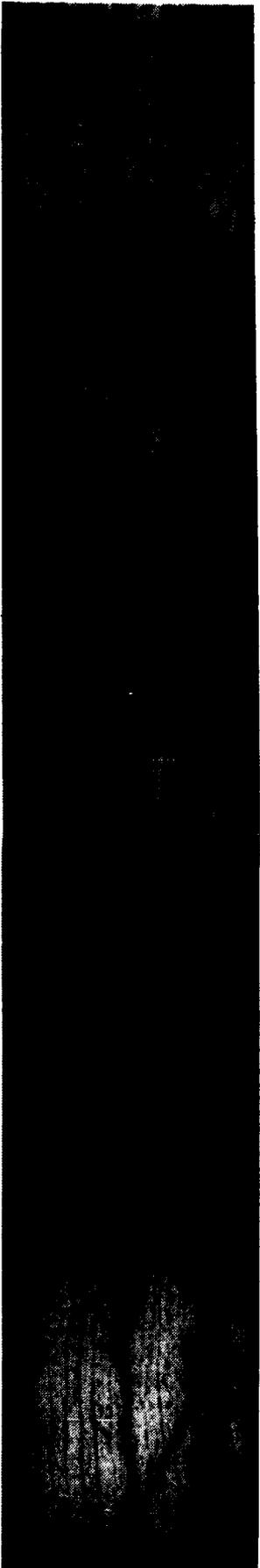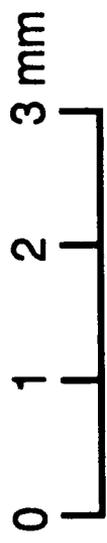
Fig. 11 - Cross section of interlaminar tension failure of a 16-ply specimen

43

outer radius

inner radius

0   1   2   3 mm
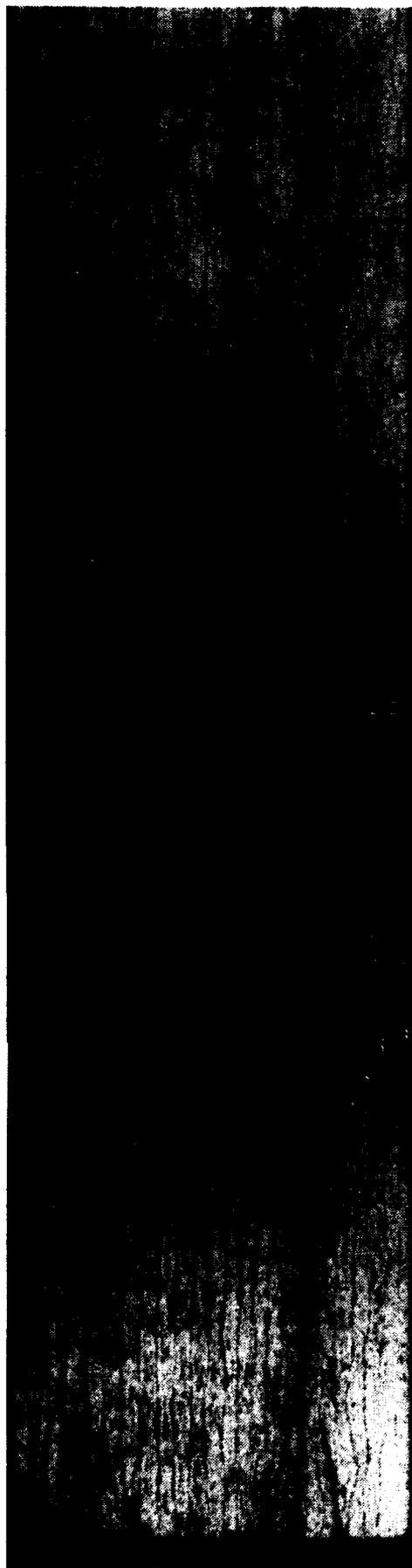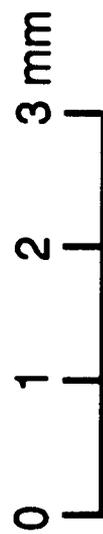
Fig. 12 - Cross section of interlaminar tension failure of a 24-ply specimen with $r_i = 3.2$ mm.

44

outer radius

inner radius

0   1   2   3 mm
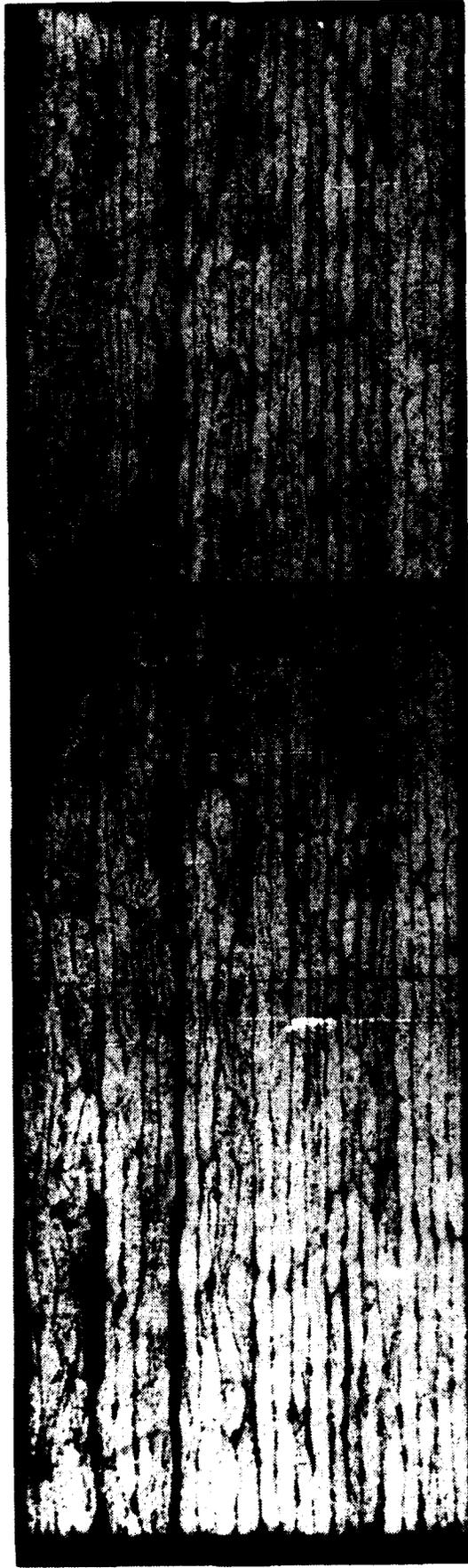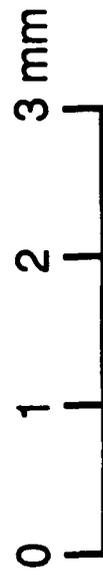
Fig. 13 - Cross section of interlaminar tension failure of a 24-ply specimen with r_i = 5.0 mm

outer radius

inner radius

initial damage

0   2   4   6 mm
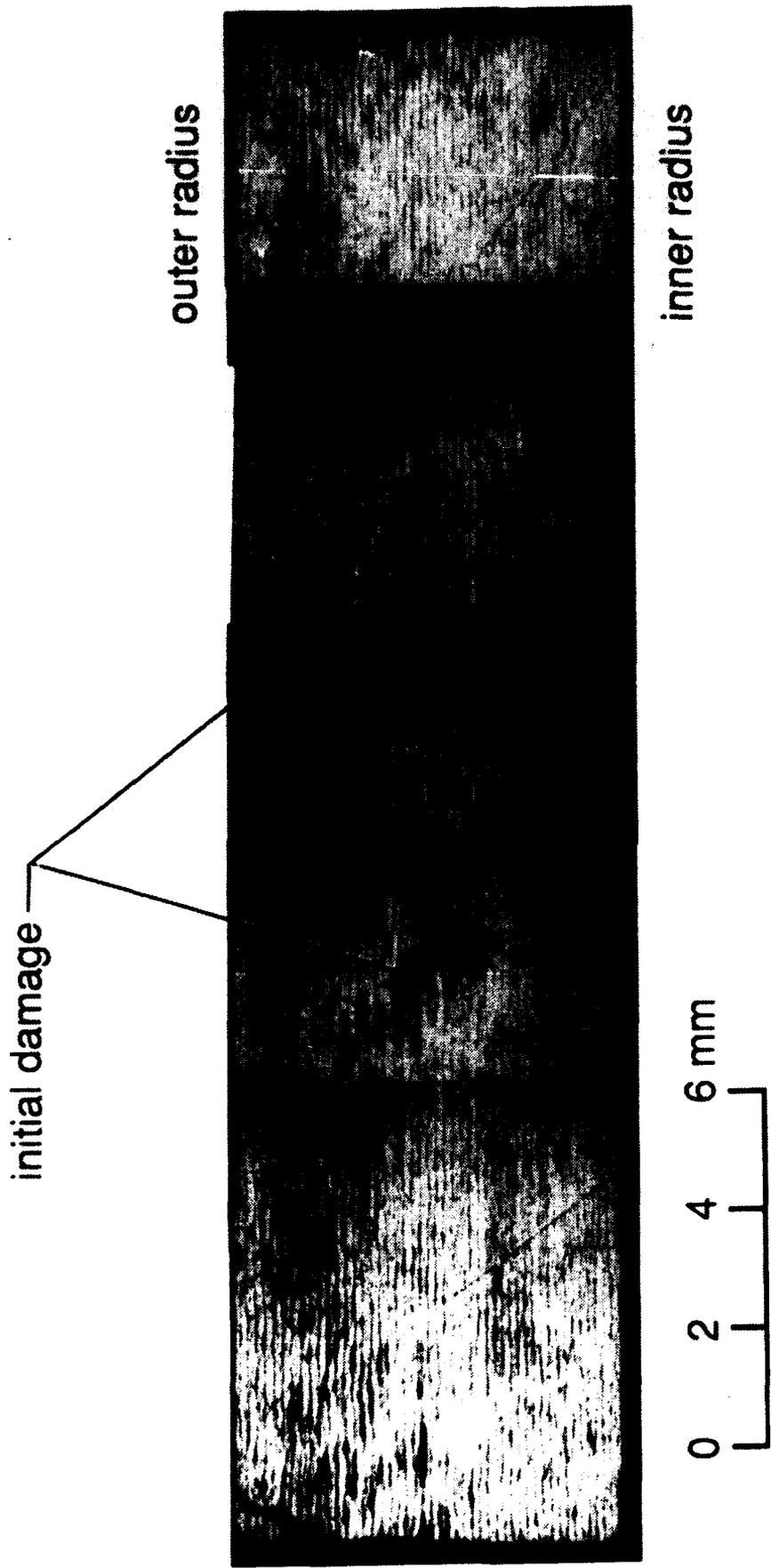
Fig. 14a - Cross section of a 48-ply specimen with initial damage

46
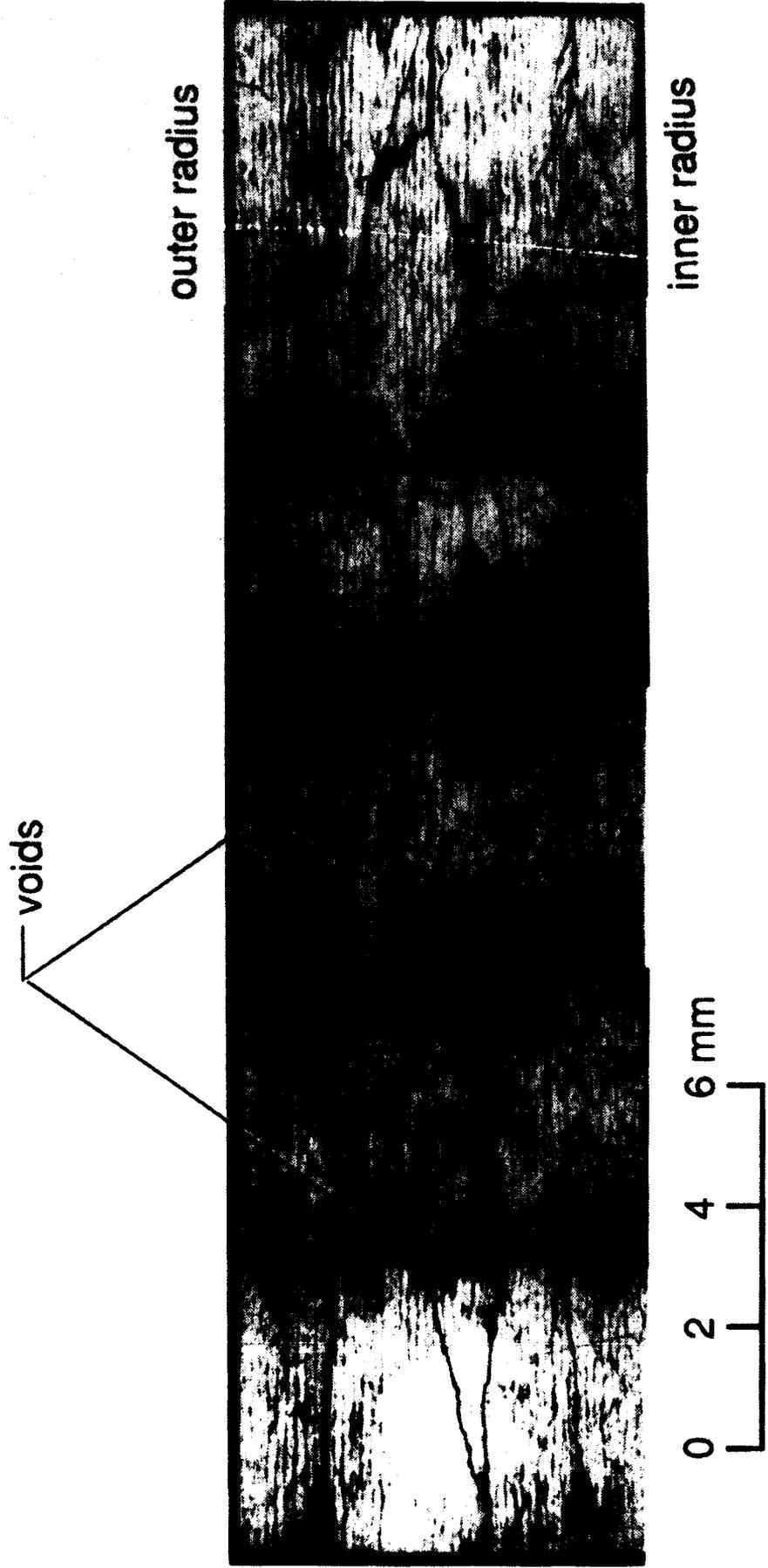
Fig. 14b - Cross section of a 48-ply specimen after final failure
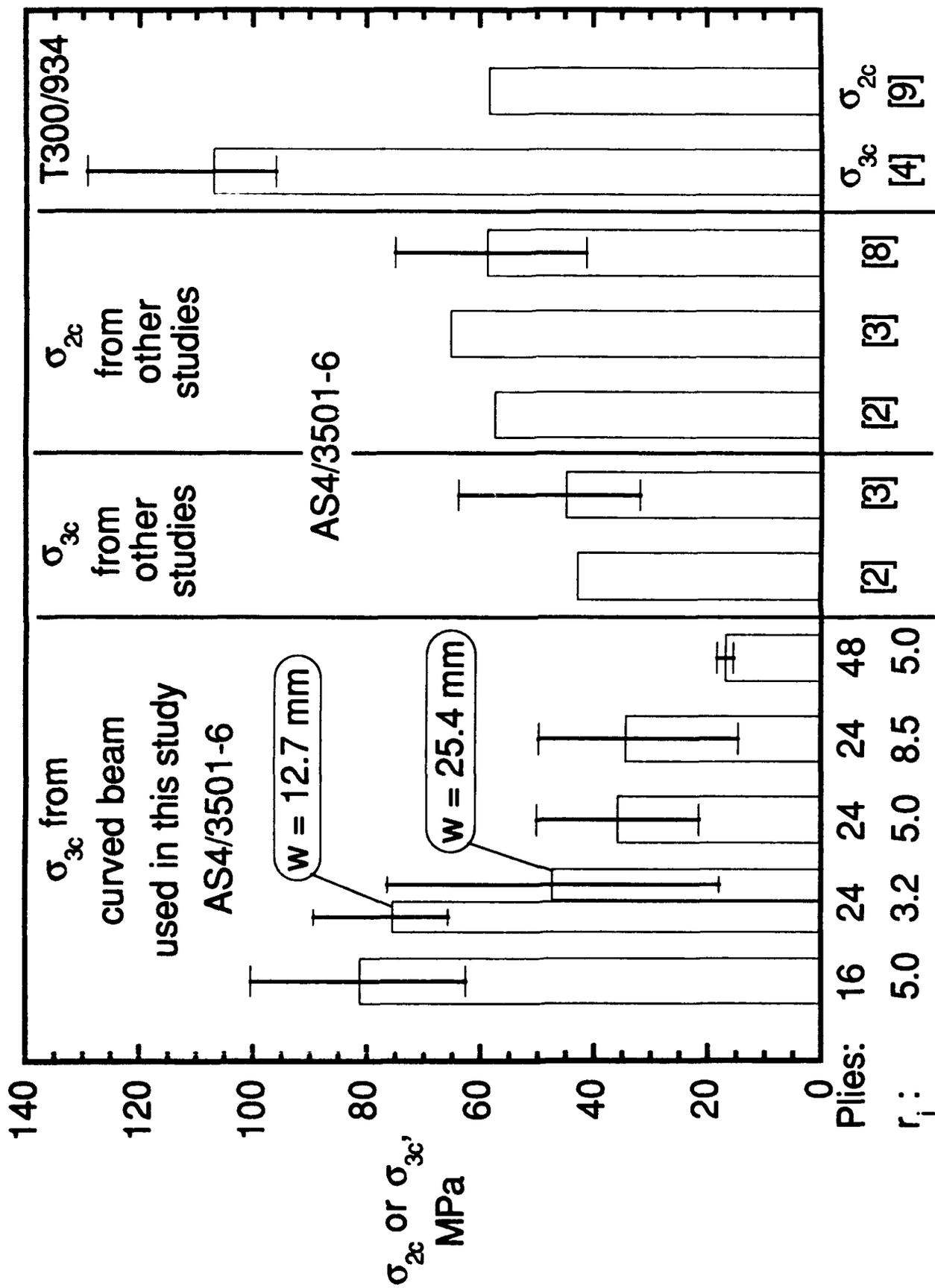
Fig. 15 - Comparison of results with other studies

REPORT DOCUMENTATION PAGE

Public reporting burden for this collection of information is estimated to average 1 hour per response, including the time for reviewing instructions, searching existing data sources, gathering and maintaining the data needed, and completing and reviewing the collection of information. Send comments regarding this burden estimate or any other aspect of this collection of information, including suggestions for reducing this burden, to Washington Headquarters Services, Directorate for Information Operations and Reports, 1215 Jefferson Davis Highway, Suite 1204, Arlington, VA 22202-4302, and to the Office of Management and Budget, Paperwork Reduction Project (0704-0188), Washington, DC 20503.

1. AGENCY USE ONLY (Leave blank)	2. REPORT DATE	3. REPORT TYPE AND DATES COVERED
	May 1992	Technical Memorandum

4. TITLE AND SUBTITLE

An Interlaminar Tension Strength Specimen

5. FUNDING NUMBERS

WU 510-02-12-10

6. AUTHOR(S)

W. C. Jackson and R. H. Martin

7. PERFORMING ORGANIZATION NAME(S) AND ADDRESS(ES)

NASA Langley Research Center
Hampton, VA 23665-5225

8. PERFORMING ORGANIZATION REPORT NUMBER

9. SPONSORING / MONITORING AGENCY NAME(S) AND ADDRESS(ES)

National Aeronautics and Space Administration
Washington, DC 20546

10. SPONSORING / MONITORING AGENCY REPORT NUMBER

NASA TM-107623
AVSCOM TR-92-B-008

11. SUPPLEMENTARY NOTES

Jackson: U.S. Army Aerostructures Directorate, NASA Langley Research Center, Hampton, VA 23665-5225;
Martin: Analytical Services and Materials, Inc., NASA Langley Research Center, Hampton, VA 23665-5225

12a. DISTRIBUTION / AVAILABILITY STATEMENT

Unclassified - Unlimited

Subject Category - 39

12b. DISTRIBUTION CODE

13. ABSTRACT (Maximum 200 words)

This paper describes a technique to determine interlaminar tension strength, σ_{3c}, of a fiber reinforced composite material using a curved beam. The specimen was a unidirectional curved beam, bent 90°, with straight arms. Attached to each arm was a hinged loading mechanism which was held by the grips of a tensile testing machine. Geometry effects of the specimen, including the effects of loading arm length, inner radius, thickness, and width, were studied. The data sets fell into two categories: low strength corresponding to a macroscopic flaw related failure and high strength corresponding to a microscopic flaw related failure. From the data available, the loading arm length had no effect on σ_{3c}. The inner radius was not expected to have a significant effect on σ_{3c}, but this conclusion could not be confirmed because of differences in laminate quality for each curve geometry. The thicker specimens had the lowest value of σ_{3c} because of poor laminate quality. Width was found to affect the value of σ_{3c} only slightly. The wider specimens generally had a slightly lower strength since more material was under high stress, and hence, had a larger probability of containing a significant flaw.

14. SUBJECT TERMS

Composite material; Carbon epoxy; Interlaminar tensile strength;
Curved beam; Delamination

15. NUMBER OF PAGES

49

16. PRICE CODE

A03

17. SECURITY CLASSIFICATION OF REPORT	18. SECURITY CLASSIFICATION OF THIS PAGE	19. SECURITY CLASSIFICATION OF ABSTRACT	20. LIMITATION OF ABSTRACT
Unclassified	Unclassified		

NSN 7540-01-280-5500

Standard Form 298 (Rev 2-89)
Prescribed by ANSI Std Z39-18
298-102